Acta Materialia 200 (2020) 74–90

Contents lists available at ScienceDirect

Acta Materialia

journal homepage: www.elsevier.com/locate/actamat

Full length article

Influence of $M_{23}C_6$ carbides on the heterogeneous strain development in annealed 420 stainless steel

J. Hidalgo[a,*], M. Vittorietti[b,c], H. Farahani[a,d], F. Vercruysse[e], R. Petrov[a,e], J. Sietsma[a]

[a] Department of Materials Science and Engineering, Delft University of Technology, Mekelweg 2, Delft 2628 CD, the Netherlands
[b] Department of Applied Mathematics, Delft University of Technology, Van Mourik Broekmanweg 6, Delft 2628 XE, the Netherlands
[c] Materials Innovation Institute (M2i), Van Mourik Broekmanweg 6, Delft 2628 XE, the Netherlands
[d] Now at Tata Steel Research Development and Technology, IJmuiden, the Netherlands
[e] Department of Electromechanical, Systems & Metal Engineering, Ghent University, Technologiepark, 46, 9052 Ghent, Belgium

ARTICLE INFO

Article history:
Received 6 March 2020
Revised 7 July 2020
Accepted 27 August 2020
Available online 2 September 2020

Keywords:
Stainless Steel
$M_{23}C_6$ carbides
plastic strain gradient
representative volume element
finite element crystal plasticity

ABSTRACT

Understanding the local strain enhancement and lattice distortion resulting from different microstructure features in metal alloys is crucial in many engineering processes. The development of heterogeneous strain not only plays an important role in the work hardening of the material but also in other processes such as recrystallization and damage inheritance and fracture. Isolating the contribution of precipitates to the development of heterogeneous strain can be challenging due to the presence of grain boundaries or other microstructure features that might cause ambiguous interpretation. In this work a statistical analysis of local strains measured by electron back scatter diffraction and crystal plasticity based simulations are combined to determine the effect of $M_{23}C_6$ carbides on the deformation of an annealed AISI 420 steel. Results suggest that carbides provide a more effective hardening at low plastic strain by a predominant long-range interaction mechanism than that of a pure ferritic microstructure. Carbides not only influence local strain directly by elastic incompatibilities with the ferritic matrix, but also the spatial interactions between ferrite grains. Carbides placed at the grain boundaries enhanced the development of strain near ferrite grain boundaries. However the positive effect of carbides and grain boundaries to develop high local strains is mitigated at regions with high density of carbides and ferrite grain boundaries.

1. Introduction

It is well known that strain development in metallic alloys is critically affected by the microstructural characteristics such as grain size of matrix phases as well as size, density and nature of existing precipitates. These characteristics influence the dislocation motion in the structure and play a fundamental role in the mechanical behaviour of the metallic alloys.

Understanding the evolution of complicated dislocation structures in metals and their effect on the hardening behaviour of the materials during deformation is a major issue in materials science. Dislocations are commonly categorized into redundant and non-redundant dislocations, respectively called Statistically Stored Dislocations (SSDs) and Geometrically Necessary Dislocations (GNDs). GNDs share similar Burgers vector and they allow the accommodation of lattice curvature due to non-homogeneous deformation. The exact manner in which GNDs contribute to the strengthening of materials is not completely understood. Existing GNDs locally interact with moving dislocations by forming jogs that provide macroscopic isotropic hardening under strain development [1,2]. Pile-ups of GNDs also lead to the development of long-range back stresses, which result in kinematic hardening [3]. The relative significance of each mechanism varies with the overall imposed strain and size of microstructure elements related to material strengthening [2].

The literature relating the microstructure to the properties via the development of GNDs in metal alloys is abundant [4–9]. GNDs typically accumulate at the grain boundaries due strain incompatibilities of grains with different orientation or constituents with dissimilar properties such as hard precipitates in a soft metal matrix. The relation between GNDs and grain size has both theoretical and experimental validations and it can be linked to the well-known Hall-Petch effect [9,10], considering that at small grain size, the grain boundary layer in which GNDs typically accumulate encompasses a relatively large volume fraction of the material [6]. The relation between hard precipitates and GNDs in metal alloys is

* Corresponding author.
E-mail address: J.HidalgoGarcia@tudelft.nl (J. Hidalgo).

https://doi.org/10.1016/j.actamat.2020.08.072

still unclear. Karamched et al. [5] showed for single crystal superalloy that GND density increases with the magnitude of imposed strain. In their study they observed that the GND density was significantly higher near the elongated carbide particles than in the matrix. However, in most common polycrystalline metals with disperse carbides, the evaluation of the relation between carbides and GNDs is not trivial because the presence of grain boundaries might cause ambiguous interpretation.

It was extensively reported that large-size carbides and other brittle particles have a notably adverse effect on the low-temperature toughness because they improve the formation and propagation of micro-cracks [11,12]. De Cock et al. [13] proposed that coarse cementite carbides develop a deformation zone with a high dislocation density, which promotes the formation of a recovered and equiaxed ferritic matrix. Vivas et al. [14] suggested a similar mechanism induced by coarse $M_{23}C_6$ carbides to explain the formation of fine equiaxed ferrite grains in ferritic/martensitic chromium steel during creep tests. These regions with high population of large $M_{23}C_6$ carbides and small size ferrite grains with low angle boundaries tend to develop microcavities, worsening the material performance to creep. It is, therefore, necessary to study and understand the local strain enhancement and lattice distortion resulting from different microstructure features, i.e. grain boundaries, precipitates or a combination of both, because they not only play an important role in the work hardening of the material but also in other processes such as recrystallization and damage inheritance and fracture.

In this work, we study the effect of large $M_{23}C_6$ carbides in the local strain development and strain hardening of an annealed AISI420 stainless steel. To isolate the effect of carbides from ferrite grain boundaries, two approaches are followed. As a first approach, real material is subjected to interrupted tensile tests at different strain levels and the development of local strain arising from different microstructure features is characterized by electron backscatter diffraction (EBSD). The second approach uses a digital recreation of the microstructure with different 3D representative volume elements (RVE) and crystal-plasticity based simulation of the strain development in the microstructure under uniaxial tensile deformation using DAMASK software [15].

2. Microscopic modelling based on crystal plasticity

The strain and stress development in different digital recreations of the microstructure was simulated combining a crystal plasticity model and the spectral solver based on FFT (Fast Fourier Transform) provided by DAMASK software. Here, only the constitutive equations for the elastic and plastic deformation are broadly presented. For a complete description of simulation procedure, the reader is referred to Refs. [15,16]. The intricate stress interactions between the grains of a polycrystalline material are modelled numerically using the spectral element (SE) method. Each grain is represented by one or more finite elements, and the polycrystal is subjected to boundary conditions that simulate the deformation under specific constraints. The single crystal plasticity model is combined into the SE framework to define the constitutive relation at each integration point of the element. The deformation in the continuum theory of crystal plasticity is described as a multiplicative decomposition into elastic, $\boldsymbol{F}_e$, and plastic, $\boldsymbol{F}_p$, parts of the deformation gradient $\boldsymbol{F}$, where the elastic part accounts for lattice distortion and rotation, and plastic distortion arises due to slip:

$$\boldsymbol{F} = \boldsymbol{F}_e\boldsymbol{F}_p \tag{1}$$

The stress at the elastic strain regime is expressed in form of the 2nd Piola-Kirchhoff stress $\boldsymbol{S}$, and depends only on the elastic strain expressed as the Green–Lagrange strain tensor $\boldsymbol{E}$ and the material specific stiffness C, according to

$$\boldsymbol{S} = C : \boldsymbol{E} \tag{2}$$

$$\boldsymbol{E} = 1/2\left(\boldsymbol{F}_e\boldsymbol{F}_e^T - 1\right) \tag{3}$$

For cubic crystals in this study, the elastic stiffness matrix is composed of three independent terms, C_{11}, C_{12} and C_{44}. It is worth to note that reversible dislocation glide, i.e. dislocation anelasticity, is not considered in the model. The evolution of plastic strain is given by:

$$\dot{\boldsymbol{F}}_p = \boldsymbol{L}_p\boldsymbol{F}_p \tag{4}$$

where $\boldsymbol{L}_p$ is the plastic velocity gradient. A widely adopted phenomenological description for the hardening is used in the present work, which is based only on slip of multiple slip systems β_i . The evolution of critical shear stress, $\dot{\tau}_C^{\beta}$, i.e. the hardening, of individual slip systems in a single crystal is given by:

$$\dot{\boldsymbol{\tau}}_{\boldsymbol{C}}^{\boldsymbol{\beta}} = \sum_{\eta} \boldsymbol{h}_{\beta\eta}\dot{\boldsymbol{\gamma}}^{\eta} \tag{5}$$

The instantaneous slip-system hardening moduli $h_{\beta\eta}$, in general, depend on the history of slip and provides information about additional hardening caused by interactions of fixed slip systems β and active slip systems η. $h_{\beta\eta}$ is determined by

$$\boldsymbol{h}_{\beta\eta} = \boldsymbol{q}^{\beta\eta}\left[\boldsymbol{h}_0\left(1 - \boldsymbol{\tau}_{\boldsymbol{C}}^{\eta}/\boldsymbol{\tau}_{\boldsymbol{sat}}\right)^{\boldsymbol{a}}\right] \tag{6}$$

The parameters h_0, τ_C^{η} and τ_{sat} are respectively the reference hardening, the critical slip resistance and the saturation shear stress, and depend on the crystal structure and the slip system. The parameter a, typically $a \geq 1$, has not a direct physical meaning, but has a direct influence on the development of hardening. The latent hardening parameter, $q^{\beta\eta}$, defines the interaction between system β and η and is set to 1, if β and η are coplanar, otherwise $q^{\beta\eta} = 1.4$. The shear strain rate $\dot{\gamma}^{\eta}$ of the system η is restricted by it resolved shear stress, τ^{η}, and τ_C^{η}:

$$\dot{\gamma}^{\eta} = \dot{\gamma}_0\left|\tau^{\eta}/\tau_C^{\eta}\right|^{1/n} sign(\tau^{\eta}) \tag{7}$$

where n is related to the strain rate sensitivity of slip and $\dot{\gamma}_0$ is the reference shear rate, being both material-specific variables. The exponent n is usually used as a numerical variable to approximate the Schmidt law and has no physical meaning. The shear rates of all slip systems can be then used to determine the plastic velocity gradient:

$$L_p = \sum_{\beta=1}^{N} \dot{\gamma}^{\eta}\boldsymbol{m}_{\beta} \otimes \boldsymbol{n}_{\beta} \tag{8}$$

where N denotes the number of slip systems ($N = 12$ for iron $\{110\}_{bcc}$ based on [17,18] and 12 for $M_{23}C_6$ carbide $\{111\}_{fcc}$), $\boldsymbol{m}$ the normalized slip direction and $\boldsymbol{n}$ the unit normal of the slip plane.

3. Experimental procedure

The AISI 420 steel used in this study contains 0.32 wt.% C, 0.2 wt.% Si, 0.3 wt.% Mn and 13.7 wt.% Cr and it was received in the form of fully annealed sheets of 0.45 mm thickness. Sub-size tensile test specimens following the ASTM E8/E8M−13a standard [19] and miniature tensile test specimens, with dimensions shown in Fig. 1, were machined with the long axis (gauge section) oriented along the sheet rolling direction. Sub-size specimens were tested in an Instron 5500R electromechanical tensile test machine, with load cell of 50 kN, at room temperature and in extension control mode. A clip-on extensometer with knife-edges, a gauge length of 7.8 mm and a maximum extension of ±2.5 mm was used to

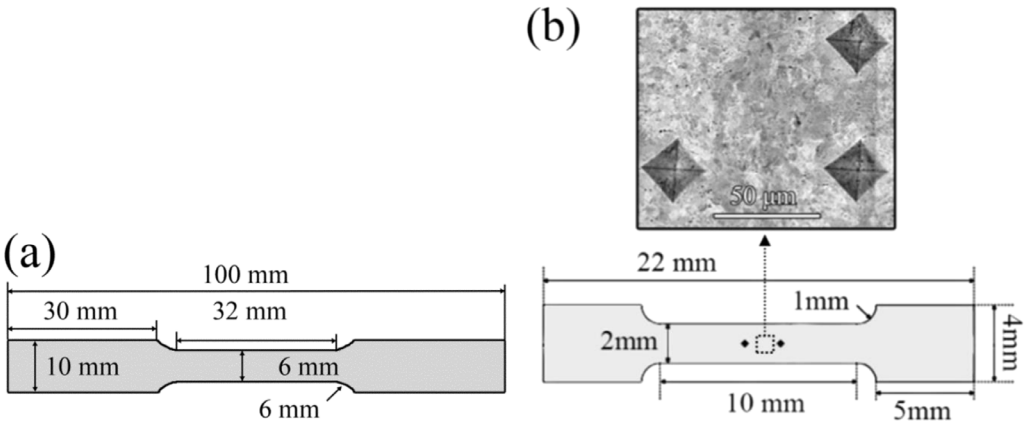

Fig. 1. Drawings of the different tensile specimens dimensions, (a) sub size specimen according to the ASTM E8/E8M−13a [19], (b) miniature specimen in wich indentations to delimit inspection area and determine plastic strains are indicated.

record the elongation during the tensile test. Three strain rates, 0.01 s^{-1}, 0.001 s^{-1} and 0.0001 s^{-1}, were applied to evaluate the strain rate sensitivity.

Miniature specimens were subjected to interrupted tensile tests to approximately 0.5 mm, 10 mm and 15 mm of cross-head displacement in a Deben micromechanical tester. The plastic strain achieved in each deformation step has been derived by the change in length between the centre of two indents placed along the gauge and separated by 1 mm distance, as shown in Fig. 1b. These indents were made by a position-controlled Vickers hardness tester applying a load of 1 N. Extra indents were made to delimit a square area of approximately 60 × 50 μm^2 upon which EBSD analysis was conducted in the unstrained condition and after each deformation step. Previous to the interrupted test and after making the indents, the top surface of the tensile specimen was prepared following the same procedure as for microstructure characterization by EBSD. This procedure consists of grinding and polishing the specimens with a final polishing step to 0.03 μm colloidal silica solution during 60 min to mitigate the plastic strains introduced at the surface during the process.

A FEI Quanta 450 scanning electron microscope equipped with a Field Emission Gun (FEG-SEM) and EDAX-TSL, OIM Data Collection software were used to obtain EBSD patterns. The set-up conditions are detailed as: acceleration voltage of 20 kV, spot size #5 corresponding to beam current of 2.4 nA, working distance of 16 mm, tilt angle of 70°, and step size of 50 nm in a hexagonal scan grid. Plasma cleaning step was carried out before each EBSD test to make sure that no changes in indexation was caused by pollution/damage of the sample due to an earlier scan. Post-processing and analysis of the orientation data was performed with TSL OIM® Analyses 6.0 software. A grain confidence index (CI) standardization was applied to the raw data, with a minimum tolerance angle and grain size of 5° and 6 pixels respectively. It was considered that grains are formed by multiple pixel rows. Thereafter, neighbour-orientation correlation with a tolerance angle of 5° and a minimum confidence index of 0.1 was implemented.

Microstructure of the samples was additionally characterized by a Field Emission Gun (FEG-SEM) JEOL JSM-6500F Scanning Electron Microscope (SEM) using the Secondary Electron Imaging (SEI) detection mode. Specimens were polished to 1 μm diamond paste and etched by waterless Kalling's reagent [20] for SEM characterization. A Bruker D8 Advance diffractometer in Bragg-Brentano geometry and with graphite monochromator and Vantec position sensitive detector was used for identifying and characterizing the precipitates observed in the microstructure. Co K_α radiation, 45 kV and 35 mA were used in the 2θ scan from 30° to 130° with a step size of 0.021° and counting time per step of 3 s. The specimen was rotated at 30 rpm during the measurement to minimise possible texture effects.

4. Results

4.1. Characterization of the initial microstructure and RVE Generation

In order to recreate simulation RVEs as closely as possible representing the real material, the initial microstructure of the steel was extensively studied and quantified using EBSD and XRD. The microstructure of annealed AISI 420 consists of ferrite with various precipitate particles, predominantly $M_{23}C_6$ carbides and MX carbonitrides [21]. Fig. 2a shows a secondary electron image of the microstructure before deformation in which ferrite grains smaller than 10 μm are highly populated with precipitates. Large round precipitates are identified as $M_{23}C_6$ Fe-Cr carbides by energy dispersive X-ray spectroscopy (EDS). This was confirmed by X-ray diffraction (XRD) analysis. $M_{23}C_6$ diffraction peaks are clearly resolved in the diffractogram of Fig. 2b. $M_{23}C_6$ carbides mainly precipitate along prior austenite grain boundaries and boundaries with a large misorientation angle [22–24]. $M_{23}C_6$ carbides tend to coarsen easily because the solubility of iron and chromium, the major constituents in this carbide, is high. Homogeneously distributed nanometre size precipitates, likely MX nitrides, can be also distinguished within ferrite grains. The MX carbonitrides typically precipitate finely and densely in the matrix bcc phase, mainly along dislocations, and do not grow significantly at high temperatures [25]. Although not confirmed by EDS, their presence in the microstructure is detected by XRD (Fig. 2b).

The overlapped phase and image quality EBSD maps are shown in Fig. 3. White lines delimit ferrite grain boundaries with misorientation angles larger than 10°. Image quality map reveals some ferrite grains sharing boundaries with angles smaller than 10°. Ferrite exhibits a broad grain size distribution, with clusters of small equiaxed grains surrounding regions of elongated larger grains which might be a reminiscence of a recrystallized rolled microstructure. $M_{23}C_6$ carbides, identified as an FCC phase in EBSD, are stochastically distributed along the ferrite matrix. Dark spots, with low image quality, can be appreciated in the image quality map indexed as BCC phase. These spots might be emerging carbides situated in the range of the depth penetration of the electron beam or carbides that were wiped out during the sample preparation process. To account for these carbides in the quantification process, points with image quality lower than a threshold based upon bimodal distribution are filtered and added to the phase quantification. A carbide fraction of 0.032 is measured by EBSD, which is a small fraction compared to the

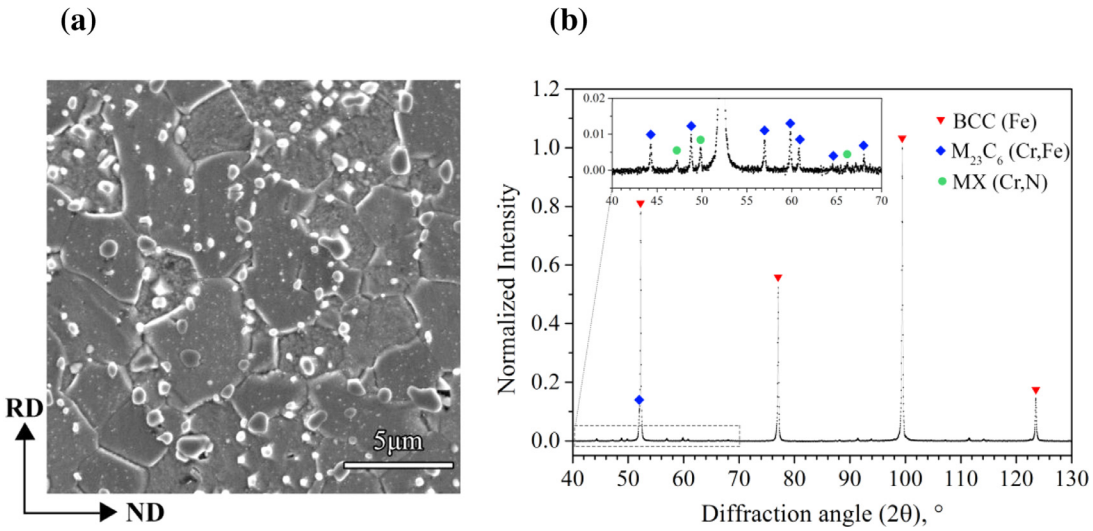

Fig. 2. (a) Secondary electron SEM image of AISI 420 in which rolling direction (RD) and normal direction (ND) is indicated. (b) XRD diffractogram in which characteristic peaks of each constituent are marked.

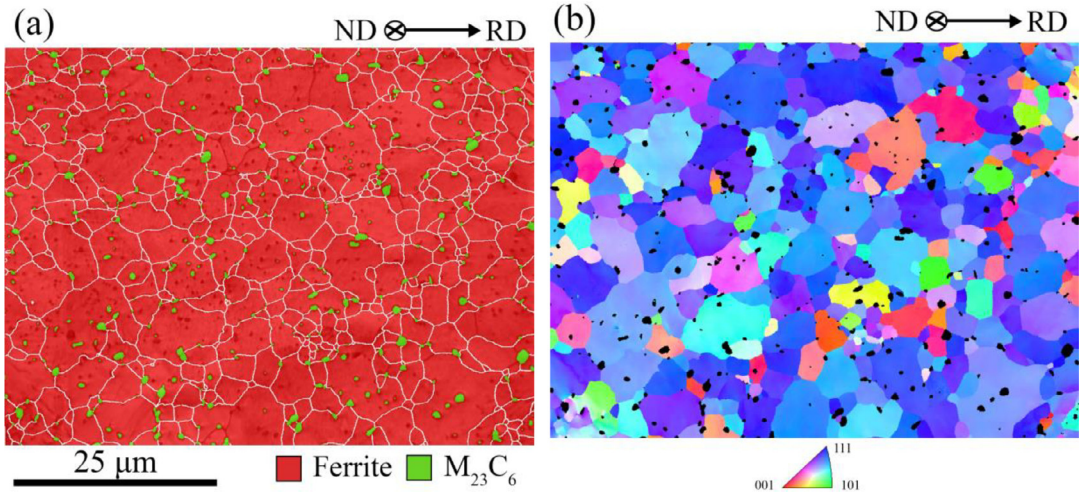

Fig. 3. (a) EBSD phase map overlapin image quality map in which white lines delimits ferrite grains with boundary angles higher than 10°. (b) ND inverse pole figure map fot the ferrite phase; black regions represent $M_{23}C_6$ carbides.

Table 1
Average grain size and shape parameters of the ferrite and carbide phases. with the corresponding standard error of the mean.

	Fraction	Grain size μm	μ	σ^2	Grain size (Area) μm	D_b/D_a	D_c/D_a
Ferrite	0.968	2.58±0.05	0.93±0.04	0.55±0.02	4.43±0.07	0.58±0.01	0.51±0.01
Carbide	0.032	0.45±0.03	0.56±0.03	0.067±0.003	0.70±0.03	0.60±0.01	0.53±0.01
	0.11*						
IG	0.47	0.26±0.01	0.38±0.02	0.028±0.001			
GB	0.53	0.54±0.03	0.48±0.06	0.039±0.003			

* Measured by XRD.

0.11±0.01 estimated by XRD. MX precipitates have FCC lattice and might be confounded with $M_{23}C_6$ carbides. However, the estimated size by SEM analysis falls below the 50 nm EBSD step size, and presumably cannot be resolved by this technique. A threshold of 6 kernels (for a size larger than 100 nm) is adopted for grain identification to avoid accounting these precipitates as $M_{23}C_6$ carbides.

The size distributions of ferrite grains and $M_{23}C_6$ carbides are shown in Fig. 4 and the relevant statistics are collected in Table 1. These values were obtained from several EBSD maps from surfaces perpendicular to the normal and transverse direction. More than 1000 grains were included in the analysis. The results were fitted to a lognormal distribution with characteristic μ and σ^2 parameters, which represent, respectively, the mean and variance of the natural logarithm of the grain size. The aspect ratio D_b/D_a and D_c/D_a of the particles were measured from normal and transverse images, where D_a, D_b, D_c represent the dimensions in the rolling, normal and transverse directions, respectively. Carbide sizes were discretized according to carbides in the grain boundaries (GB) or inside (IG) ferrite grains as shown in Fig. 4b. There is a similar

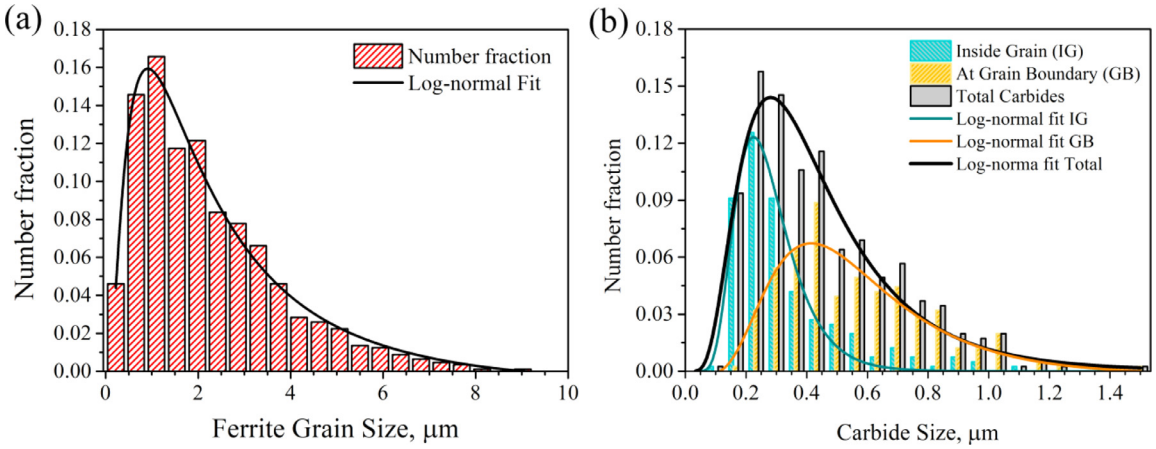

Fig. 4. (a) Histogram showing ferrite grain size distribution (b) Histogram showing carbide size distribution in which every bin is split according to the carbide is inside the ferrite grain or at the ferrite grain boundary.

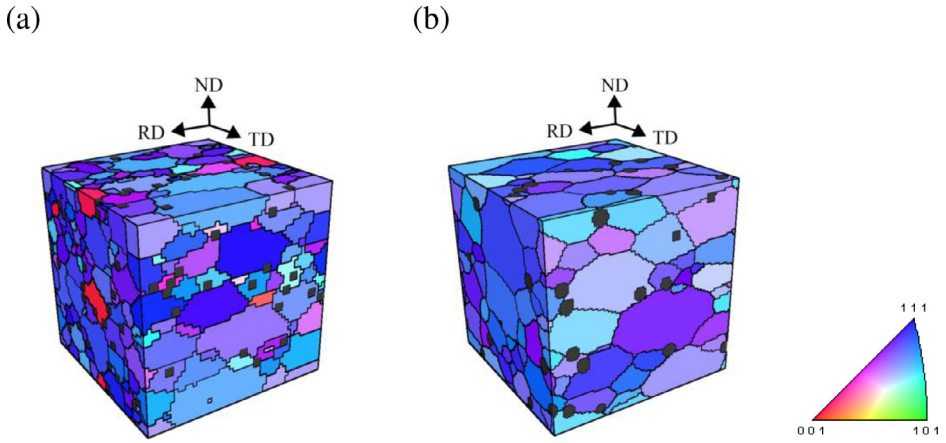

Fig. 5. Inverse pole figure map of (a) $RVE_{CARB.}$ and (b) $RVE^{*}_{CARB.}$ in which grain limits are lined in black and $M_{23}C_6$ carbides are filled in black colour.

fraction of carbides placed at GB and IG, but carbides at GB are significantly larger.

The ferrite inverse pole figure map in Fig. 3b indicates a preferential orientation of $\{111\}_{bcc}$ parallel to the normal direction, i.e. the γ fibre, which is typical for rolled steels [26]. Texture was translated in terms of an orientation distribution function (ODF), which along with the microstructure statistics was used to generate a representative volume element of AISI 420 steel microstructure by StatsGenerator filter of DREAM.3D software [27,28]. The algorithm first creates a collection of idealized ellipsoidal grains having a distribution of size, shape and shape orientation equivalent to those observed in the experimental microstructure. Secondly, the generated grains are placed inside a representative volume. A number of constraints are used to determine the arrangement and spatial location of the grains inside this volume. Thereafter, the constrained Voronoi tessellation method is employed for the creation of a Voronoi tessellation that represents the grain structure produced in previous steps in order to reduce the number of elements and possibly improve the accuracy of the boundary representation. Finally, crystallography orientations are assigned to the grains, such that the orientation and misorientation functions are statistically equivalent to the experimental dataset. Two RVEs with different resolution and number of grains were generated for specific purposes. $RVE_{CARB.}$, corresponding to Fig. 5a, with 50 × 50 × 50 voxels, 502 ferrite grains and 174 carbides, was used for calibration of material properties. $RVE^{*}_{CARB.}$, represented in Fig. 5a, with 100 × 100 × 100 voxels, 268 ferrite grains and 109 carbides, was used for the assessment of local strain development during uniaxial deformation.

4.2. Calibration of materials parameters

The calibration of the crystal plasticity constitutive parameters for ferrite, $\tau_{C,0}$, τ_{sat}, h_0, a and n, was performed based on strain-stress data from tensile test (see Fig. 6) and the implementation of a modified Nedler-Mead (NM) simplex algorithm following a similar procedure as described in [29]. NM simplex algorithm [30], outstands for its simplicity and easy implementation. Its deterministic character and independence on gradient information makes it suitable for the relatively low dimensional optimization inverse problem. The algorithm iteratively adjusts the parameters by performing crystal plasticity simulations of the uniaxial tensile deformation of RVE and comparing the resulting strain-stress data to the experimental reference. When the deviation, evaluated in the present work by the error sum of squares, meets a given tolerance, the algorithm finalises. The fitting process was performed for three strain rates to best optimise the n parameter. The bounds of calibrated parameters were defined based on typical values for ferrite presented in Table 2. There is a lack of dedicated data of ferrite parameters in stainless steel and in general for steel systems. Therefore, the bounds were largely expanded, maintaining the limits of typical values in metals. In the crystal plasticity model, plastic deformation initiates only by slip and is regulated for a single crystal by $\tau_{C,0}$. It can be considered that the calibrated value of $\tau_{C,0}$ will

Table 2
Material parameters of BCC iron and $M_{23}C_6$ carbides in single crystals.

Parameter	Unit	Ferrite Ref. [7]	Ref. [37]	Ref. [38]	Adopted	$M_{23}C_6$ Adopted
C_{11}, C_{12}, C_{44}	GPa	233, 135, 128	-	233, 135, 128	472[a], 216[a], 135[a]	
$\dot{\gamma}_0$	s^{-1}	1×10^{-6}	1×10^{-6}	1.07×10^{-6}	1×10^{-6}	1×10^{-6}
n_{slip}	-	20	10	–	**65***	200
$\tau_{C,0}$	MPa	95	200	14	**77***	1200
τ_{sat}	MPa	222	400	132	**226***	2000
h_0	GPa	1	0.8	0.7	**2.53***	20
a	–	2.25	1.5	1.5	**1.75***	1.1

[a] Ref. [31],
* Calibrated in for AISI 420 of the present study.

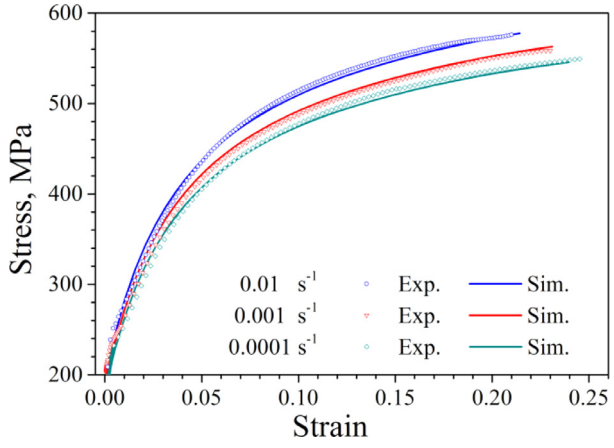

Fig. 6. Experimental (open symbols) and simulated (lines) true strain stress curves obtained at different strain rates.

effectively account for other strengthening mechanisms, e.g. presence of grain boundaries, dislocations, precipitates, etc., which also affect the material yielding. Therefore, in the polycrystal and for uniaxial tension, estimation of $\tau_{C,0}$ was made by connecting this parameter with the yield stress (σ_y) and the arithmetic mean of the Taylor factor, M, by:

$$\boldsymbol{\sigma_y = M\tau_{C,0}} \tag{9}$$

The experimental σ_y for 0.0001 s^{-1} strain rate, determined by the 0.2% offset method, resulted to be 222 MPa. The measured M for the ferrite in present steel is 2.9, which leads to a value of 76.5 MPa for $\tau_{C,0}$, applying Eq. (9). The n parameter can be worked out directly from relative comparison of the tensile curves at different strains [31]. Considering the virtual-work principle $\tau d\gamma = \sigma d\varepsilon$ applies [32], then from Eq. (7):

$$\dot{\varepsilon} = \dot{\varepsilon}_0 \left(\frac{\sigma(\dot{\varepsilon})}{\sigma(\dot{\varepsilon}_0)} \right)^n \Rightarrow \frac{\sigma(\dot{\varepsilon})}{\sigma(\dot{\varepsilon}_0)} = \left(\frac{\dot{\varepsilon}}{\dot{\varepsilon}_0} \right)^{1/n} \tag{10}$$

Applying Eq. (10) to experimental tensile curves, $n = 65$ is obtained.

Finding experimental measurements of the mechanical properties of single crystal of $M_{23}C_6$ carbide is more challenging and thus, a rather qualitative choice of material parameters has been made. Ab-initio calculation of elastic properties of different $M_{23}C_6$ carbides can be found in Liu et al. [33]. $M_{23}C_6$ carbides could be considered as rigid particles compared to the ferrite matrix. There is evidence that M_7C_3 can yield to plastic deformation at moderate temperatures, where dislocation gliding and deformation twins mechanisms operate [34], however no information was found on its yield stress. Inoue et al. [35] determined the hardness of $(Fe\text{-}Cr)_{23}C_6$ depending on several alloying elements and concluded that Mn, present in AISI 420 composition, has a minor effect. Values of 1100 HV0.3 were reported, which can be translated to 10.8 GPa [19]. Assuming that the yield strength is one third of the hardness Vickers value [36] and considering $M = 3$, $\tau_{C,0}$ results in 1200 MPa. The rest of the parameters were selected in order to emulate a particle exhibiting high hardening. Simulations revealed that despite the stress being partitioned to carbides, it did not develop to values high enough to initiate plastic deformation. Hence, the hardening related parameters, except $\tau_{C,0}$, can be considered anecdotic for $M_{23}C_6$ in the frame of the present study.

Fig. 6 shows the experimental (open symbols) and simulated (lines) true strain-stress curves obtained at different strain rates for optimised simulation parameters. The experimental strain-stress curves at different strain rates are well predicted by the crystal plasticity model using the calibrated ferrite parameters in Table 2 and RVE_{CARB}. Comparing the ferrite parameters for AIS 420 steel with the values in literature, similarities are found for $\tau_{C,0}$ and τ_{sat} with Ref. [7], which were optimised for ferrite in a dual phase steel. $\tau_{C,0}$ and τ_{sat}, also adopted for ferrite in a dual phase steel, are higher in Ref. [37], which indicates that any comparison should be done with care. Anyhow, the low $\tau_{C,0}$ and τ_{sat} values in Ref. [38] are consistent with the fact that they are for plain iron ferrite. It is worth to note that the calibrated $\tau_{C,0}$ for the present steel is close to the value estimated by Eq. (9). The reference hardening, h_0, is significantly higher in the present work compared to all consulted references, whereas a takes an analogous value to most of them. The strain rate sensitivity obtained for the studied range of strain rate is considerably lower than for ferrite in other studies as it is deduced from the high n value.

4.3. Local strain development by EBSD analysis

The local evolution of strain during tensile deformation of AISI420 microstructure was evaluated by the analysis of the Kernel Average Misorientation (KAM) parameter from EBSD scans as credited in a number of studies [39,40]. KAM accounts for the local average crystal misorientation $\Delta<\theta>$ around the distance Δx from a measurement point [41], which can be connected to the lattice curvature tensor ($\boldsymbol{\kappa}$) by the Nye tensor associated to GND density ($\boldsymbol{\alpha}$). In a simplified one-dimensional (scalar) representation and assuming only parallel edge dislocation of the same sign, this tensor relation is expressed as [42]:

$$\boldsymbol{\kappa = d\theta/dx = b\alpha/c} \tag{11}$$

where $d\theta/dx$ can be approximated as $\Delta<\theta> / \Delta x$ and b is the modulus of the Burgers vector, which is $(a/2)<111>$ for bcc lattice. The lattice parameter, a, of the ferrite phase in AISI20 steel is 2.8723±0.0001 Å, which was calculated from XRD peaks and the Nelson-Ridley method [43]. c is a constant that depends on the geometry of the boundaries, having values of 2 and 4 for pure tilt and pure twist boundaries, respectively. In reference [40], it is demonstrated that using Nye's tensor, $\alpha = 3$, which represent a mixed-type boundaries and is selected for the present study. More so-

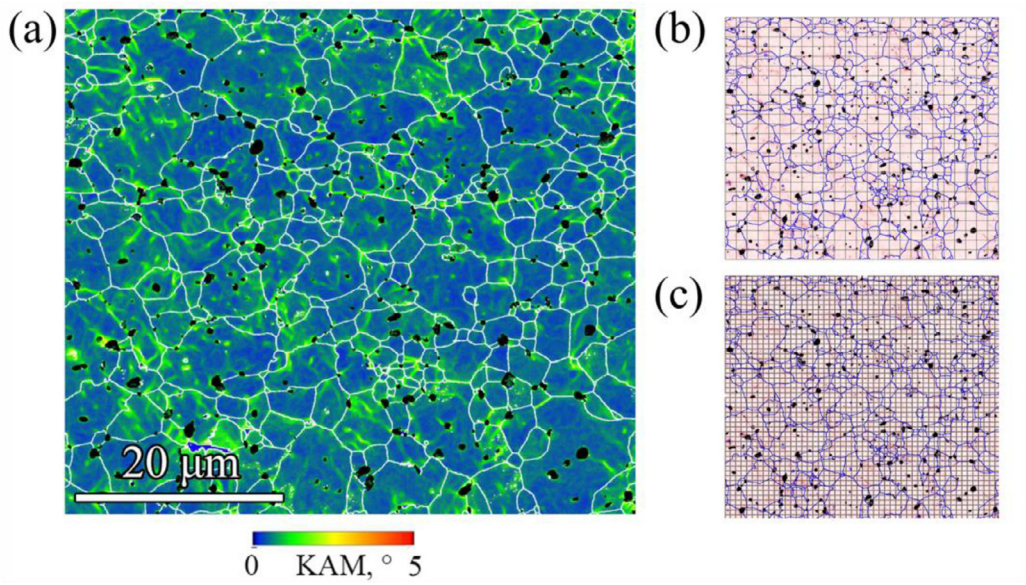

Fig. 7. (a) KAM map of ferrite phase for the 0.066 plastic strain condition. White lines delimits a threshold grain boundary misorientation of 10° and black ellipsoids represent $M_{23}C_6$ carbides. The map is parcelled in 25 × 25 (b) and 50 × 50 (c) grid for statistical analysis.

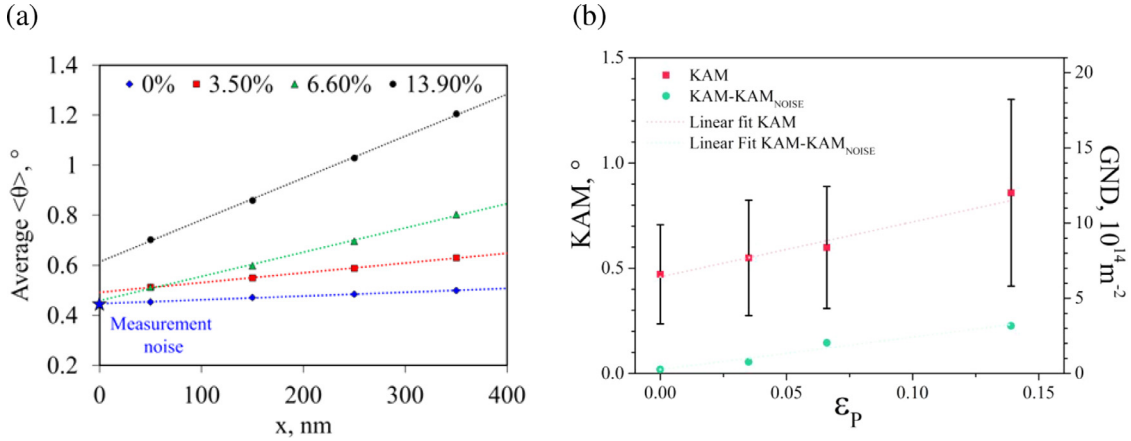

Fig. 8. (a) Average $<\theta(x)>$ with 5° upper threshold as a function of the kernel radius (1st, 3rd, 5th and 7th neighbours) calculated on an EBSD map of AISI 420 deformed to different strains. (b) Variation of average KAM with strain. Original and corrected KAM are presented and fitted to a linear equation (dashed lines).

phisticated methods considering extended components of the Nye tensor [44,45] and cross-correlation EBSD techniques for the estimation of GND density can be found in literature e.g. [5,9,46]. Although present results could potentially differ from these studies, it is likely that they would follow the same trends.

Strain heterogeneities were revealed by KAM maps at all deformation levels, as representatively shown in Fig. 7a for the 0.066 plastic strain condition. High KAM values are observed near grain boundaries (delimited by white lines) and particularly close to carbides (black ellipsoids), while low KAM values are rather more spread throughout the material. KAM is very sensitive to the EBSD step size [44,46], and the overestimation due to the measurement noise is drastically increased when decreasing the step size. The method proposed by Kamaya [47], illustrated in Fig. 8a, is used to estimate the measurement error. $<\theta(x)>$ values have been calculated for each pixel of the map using the i^{th} neighbours (i = 1, 3, 5, 7). The individual values of $<\theta(x)>$ are then averaged to obtain a representative value of the whole scan. $<\theta(x)>$ values below 5 ° are considered in the calculation to discount grain boundaries from the analysis. The average value of $<\theta(x)>$ increases linearly with the kernel radius, as shown in Fig. 8a. This is an indication of the misorientation gradient being constant in the explored neighbourhood around each pixel. The increase of the slope with the strain is explained by larger misorientation gradients as the steel is more plastically deformed. In absence of measurement noise, the extrapolated $<\theta(x)>$ values to $x = 0$ should tend to zero. In Fig. 8a, it can be observed that $<\theta(x = 0)>$ ranges between 0.4 ° and 0.6 ° at different strains, which can be considered as an estimate of the measurement noise. Assuming that under very small (shear) strains $d\gamma = \mathrm{tg}(d\theta) \approx d\theta$ and the estimated measurement noise, the shear plastic strain detection limit is in the range of 0.007 - 0.01, which falls below the chosen macroscopic plastic strains. Hence, it is considered that measurement noise is not significantly affecting evaluation of local strains by analysing KAM maps except for the unstrained condition.

Fig. 8b shows an ascending linear relation between the plastic strain and the average KAM values (or equivalent GND density by applying Eq. (10)), which up to the strain level analysed here (0.139) well reproduces the Ashby model [42] and is consistent with the observations reported by other studies on ferritic steels [44,45]. Standard deviation in the distributions of KAM was used to generate the error bars. The increase of standard devia-

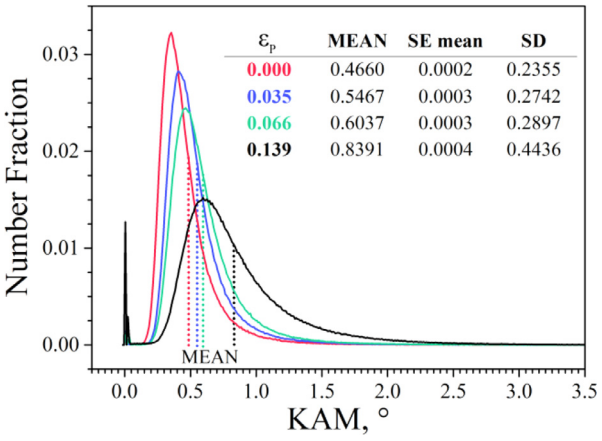

Fig. 9. KAM distribution at different macroscopic plastic strain levels for AISI 420 steel.

tion with increasing plastic strain is explained by the strain heterogeneities present in the specimens. This is evidenced by the evolution of KAM distribution with plastic strain in Fig. 9a, which appears highly skewed with a pronounced tail to the high KAM side of the peak. It is worth noting that the KAM distribution (including measurement noise) in the unstrained condition already exhibits significantly high values compared to the strained specimens. In the unstrained specimen, high KAM values are mainly concentrated at $M_{23}C_6$/ferrite interfaces (see Fig. 10), which may be explained by thermal strains arising from differences in the thermal expansion coefficients during cooling [5] or from lattice mismatch [48]. The average KAM value for the carbide phase is higher than for ferrite in the unstrained condition. This fact might be explained by a poor image quality of carbides. Nevertheless, average KAM of carbides remained nearly unaltered regardless the applied macroscopic strain, which suggests a negligible plastic deformation.

The locations where strain preferentially develops are qualitatively analysed by comparing KAM and image quality (IQ) maps in Fig. 10 at four different levels of deformation in same EBSD scan region. High KAM values locally develop primarily at carbides at low macroscopic strains. At higher strain levels, localized strain at ferrite grain boundaries and triple junctions becomes more evident, but regions with high KAM further extend to grain interior, connecting other carbides and forming a cell structure. However, it is difficult to judge the individual effect of different microstructure features due to mutual interaction and the fact that information is missing from microstructure below the specimen surface.

The formation of shear bands is detected in IQ maps from 0.066 plastic strain. The development of shear bands is less evident by analysing KAM maps. Only for a few cases, the observation of a shear band in IQ corresponds to an observation of high KAM at the surroundings. The correlation between low IQ and high KAM in the surrounding of shear bands becomes more evident as the plastic strain is increased. Shear bands are often characterized by strong lattice curvature and very high densities of geometrically necessary dislocations at the interior of the shear band and the surrounding matrix. However, it should be considered that a free surface can relax high local shears by producing a surface relief, excluding the need to accommodate heterogeneous strain by the generation of geometrically necessary dislocations. Shear bands still consist of very small dislocation cells and contain very high dislocation densities. The IQ will be more affected by surface relief and high density of SSDs than the KAM as long as the pattern is still sufficiently strong to result in trustworthy orientation data.

A statistical analysis was performed for an in-depth analysis of the microstructure features that most influence the development of local strain with deformation in the AISI 420 steel microstructure. EBSD maps are parcelled in different areas containing different microstructure features as shown in Fig. 7b and 7c. 25 × 25 and 50 × 50 grids are compared to assess the influence of the parcel area on the statistical analysis. The parcel area of unstrained condition is 4 μm^2 and 1 μm^2 for the 25 × 25 and 50 × 50 grids, respectively, which are on the order of the average ferrite grain and carbide sizes. KAM is used as a response variable for the analysis, which is a proxy of the local strains and density of GND, and is related to the presence of grain boundaries, carbides or a combined effect. Two possible explanatory variables are initially considered: number of grains (N_G) and number of carbides (N_C). The average KAM of each parcel is calculated along with N_G and N_C. A consistent population of points, in particular in measurements at high plastic strains, exhibit KAM values near zero (see Fig. 9a). These points are related to poor indexing and are filtered out by creating a reduced image with a significant and representative number of data.

The KAM box and whisker plots of N_C and N_G explanatory variables at different plastic strains are shown in Fig. 11. The box represents the quartiles 25–75%. The whiskers extend up to 1.5 times the interquartile range. The outliers are represented by hollow diamonds, with the minimum and the maximum of the distribution indicated as solid diamonds. Solid squares represent the average KAM of the population and dotted horizontal lines denote the average KAM of the whole map.

Focusing on the unstrained condition and comparing the boxes of the explanatory variables, it can be clearly seen that KAM increases with the number of grains and the number of carbides. In absence of carbide or when there is no grain boundary, i.e. N_G equals one, the average KAM of the population is below the average KAM value of the scan. These effects are more prominent in the case of 50 × 50 grid and indicate the localization of high KAM values around ferrite grains and carbides. As previously discussed, these observations are explained by strains induced during cooling due to differences in the coefficient of thermal expansion of ferrite and $M_{23}C_6$ carbides and due to a mismatch between the grains' crystallography [5,48].

KAM increases with plastic strain. This statement holds for all populations as highlighted in Fig. 11. The presence of carbide typically results on higher KAM compared to the condition without carbides, which is equivalent to or exceeds the average value of the scan. KAM increases with the number of carbides. The same statement applies for parcels with high population of grains, but the effect is less noticeable. The difference between the average KAM of different populations of N_G and N_C decreases with plastic strain. This fact is more obvious in the results of 50 × 50 grid. Moreover, the increase of KAM with plastic strain is less pronounced for high numbers of N_G and N_C. The influence of individual explanatory variables on the evolution of KAM with plastic strain compared to others is difficult to assess by only looking at the plots in Fig. 11 because of the combined effects of N_G and N_C. The following multivariate linear regression model, which includes the macroscopic plastic strain ε_P, is fitted:

$$KAM = K_0 + K_1\varepsilon_P + K_2\left(\frac{N_G}{A}\right) + K_3\left(\frac{N_C}{A}\right) + K_4(N_G N_C/A^2) \qquad (12)$$

with K_i/i = 0, 1, 2, 3, 4 are the model coefficients and A the parcel area. K_0 is the intercept and represents the average KAM in the case of unstrained condition for the ferrite phase without carbides or grain boundary contribution. The interaction of NC and NG is introduced by the last term. Table 3 collects the resulting coefficients after applying multilinear regression analysis based on

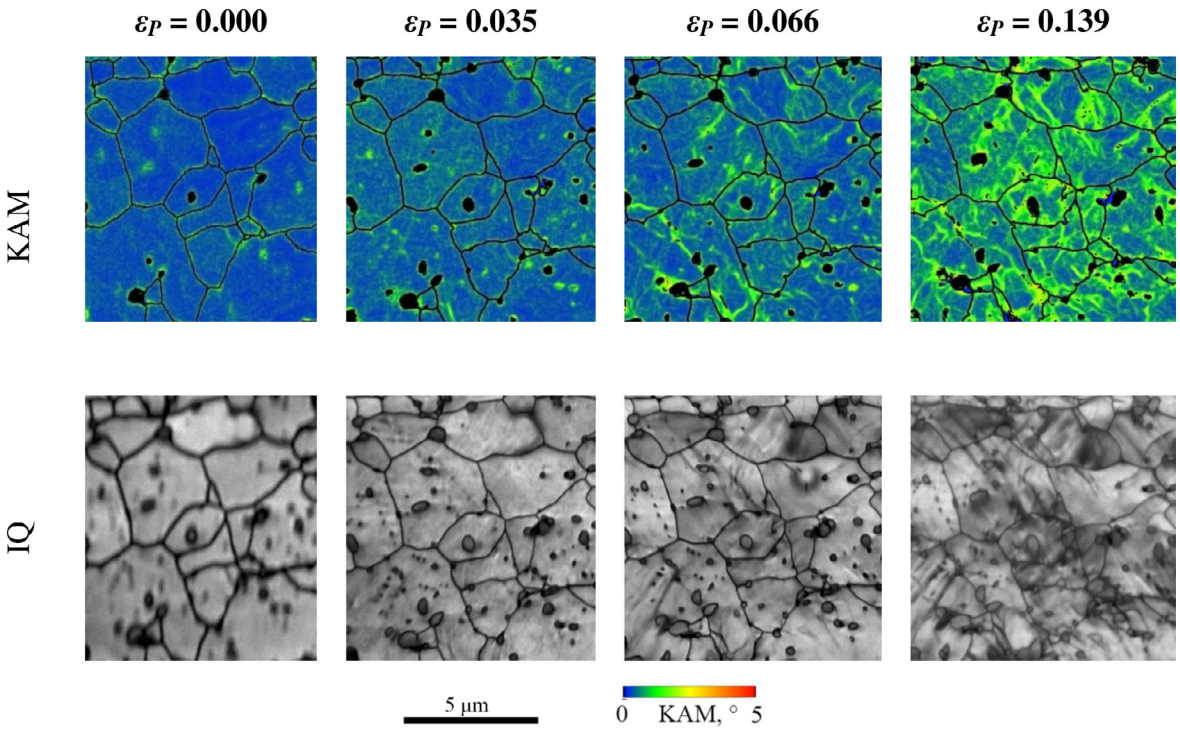

Fig. 10. KAM and IQ at different macroscopic plastic strains for the same region of AIS 420 steel.

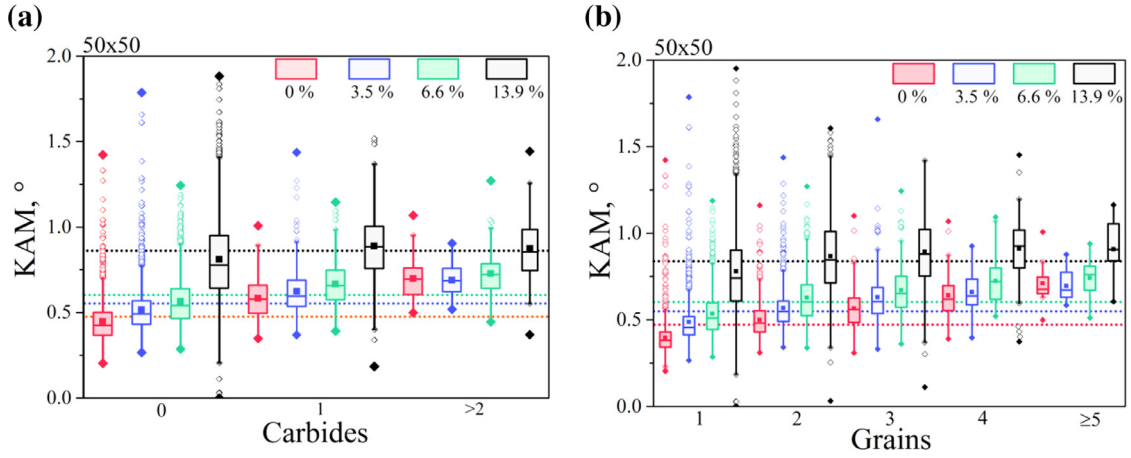

Fig. 11. Box and whisker plots of different explanatory variables, (a) number of carbides and (b) number of grains corresponding to 50 × 50 grid.

Table 3
Coefficients after applying multilinear regression analysis of Eq. (11).

	K_0 (Intercept) (°)	K_1~ε_P (°)	K_2~N_G/A (μm^2)	K_3~N_C/A (μm^2)	K_4~$N_G N_C/A_2$ (μm^4)
50 × 50					
Estimate	0.320	2.59	0.041	0.072	−0.010
Std. Error	0.004	0.03	0.001	0.004	0.001
t value	78.6	85.9	34.2	15.9	−8.1
Pr (>|t|)*	$<2\bullet10^{-16}$	$<2\bullet10^{-16}$	$<2\bullet10^{-16}$	$<2\bullet10^{-16}$	$<2\bullet10^{-16}$
25 × 25					
Estimate	0.360	2.60	0.078	0.09	−0.04
Std. Error	0.007	0.05	0.006	0.02	0.01
t value	54.8	55.6	13.9	5.05	−3.1
Pr (>|t|)*	$<2\bullet10^{-16}$	$<2\bullet10^{-16}$	$<2\bullet10^{-16}$	$5\bullet10^{-7}$	0.002

* Pr (>|t|) evaluates the significance of the explanatory variable on the model. Values approaching zero indicates high significance. $R^2_{25x25} = 0.59$; $R^2_{50x50} = 0.49$.

Table 4
Codes for the variable CP which classify EBSD grid parcels according to the observed microstructure features.

0	No carbides
1	Inner carbide
2	Carbide in the boundary between two grains
3	Carbide in the boundary between three grains, i.e. a triple point
12	Two carbides: one inner carbide and one in the boundary between two grains
13	Two carbides: one inner carbide and one in the boundary between three grains
23	Two carbides: one carbide in the boundary between two grains and one in the boundary between three grains
123	Three carbides: one inner carbide, one in the boundary between two grains and one in the boundary between three grains

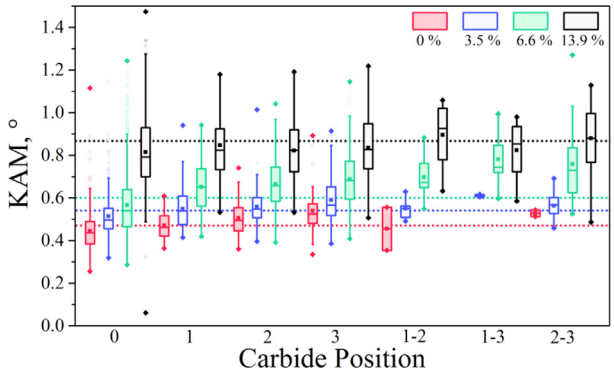

Fig. 12. Box and whisker plots showing the evolution of the mean kernel average misorientation (KAM) with plastic strain an as a function carbide position in the microstructure as defined in Table 4.

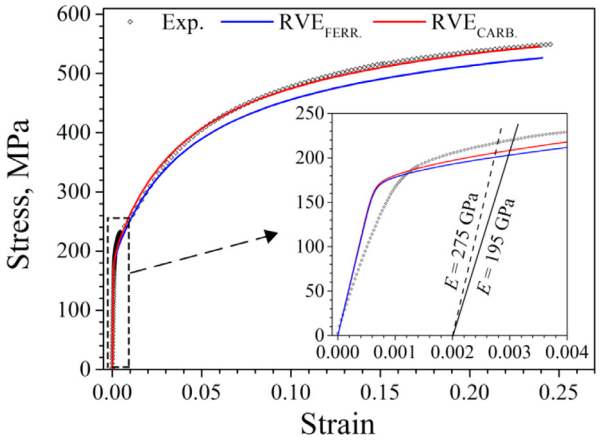

Fig. 13. True strain true stress curves obtained from experimental (Exp.) and modelled ($RVE_{CARB.}$ and $RVE_{FERR.}$) tensile tests.

model of Eq. (11), along with the standard error and significance parameters.

From the linear regression model it can be observed that K_0 is on the order of the measurement noise, which means that mean KAM should tend to 0 in absence of grain boundaries and carbides, which is what is physically expected. The high values of K_1 indicate that KAM is primarily influenced by strain, and the value of 2.6° matches well with the slope of linear relation of KAM with plastic strain presented in Fig. 11. The increase of KAM with the number of carbides (i.e. carbide density) is more effective than with the number of grains (i.e. grain boundary density), as resulting from comparing K_2 and K_3, but this is only evident in the 50 × 50 grid. The positive effect of these variables was expected from the analysis of box and whisker plots. However, the negative sign associated with the interaction parameter K_4 means that the regions with high density of grain boundaries and carbides will counteract the development of KAM by the positive effect of K_2 and K_3.

Former analyses disregard the influence of the position of carbides in the microstructure on the intensity of KAM. Grid parcels in the EBSD map were classified according to the position of carbides by a categorical variable, CP, which is coded as described in Table 4. Fig. 12 shows the KAM box and whisker plots of CP. There is a clear dependence on carbide position in the development of KAM. Average KAM is enhanced when the carbides are positioned at ferrite grain boundaries and specially at triple points (CP = 2, 3) compared to carbides inside ferrite grains (CP = 1). This fact points to a magnified effect on the development of local strains due to a combined action of carbides and grain boundaries. Taupin et al. [49] discussed the thickness of a layer with increased GND density in a ferritic steel with spheroidized cementite. Their results showed that when the cementite diameter is at micron scale, the thickness of GND layer is independent of carbide size. Ma et al. [50] argued, however, that when cementite diameter is at submicron size, as it is the case of the present study, a ratio should be maintained between the thickness of GND layer and the diameter of the particle. Average size of intragrain $M_{23}C_6$ carbides is smaller than that of carbides at grain boundaries, which might explain the lower values of average KAM. Nevertheless, average KAM in parcels containing carbides at grain boundaries is typically higher than that in parcels in which only grain boundaries were recorded. From Fig. 12, it is also observed that the average KAM of different CP at high plastic strains tends to equal with NG and NC.

4.4. Isolation of carbide effect by model microstructures

The effect of carbides on the mechanical response is evaluated by a new representative volume element, $RVE_{FERR.}$, sharing the microstructure topology and texture with $RVE_{CARB.}$, but in which material properties for the $M_{23}C_6$ carbide are substituted for those of ferrite phase. Any difference in the crystal plasticity modelling between RVE_{FERR} and $RVE_{CARB.}$ will consequently be attributed only to an incompatibility arising from a mismatch in the strength between two phases.

Fig. 13 shows the strain and stress curves after tensile deformation of $RVE_{CARB.}$ and $RVE_{FERR.}$ with a strain rate of 0.0001 s^{-1}. Differences in the yielding of $RVE_{CARB.}$, $RVE_{FERR.}$ are insignificant. However, the initial hardening rate of $RVE_{CARB.}$ is slightly higher than that of $RVE_{FERR.}$, which results in a lower ultimate tensile strength in $RVE_{FERR.}$ Fig. 14a shows the distribution of equivalent Von Mises strain for the ferrite phase in $RVE_{CARB.}$ and $RVE_{FERR.}$ at macroscopic plastic strains similar to those of the experimental tests. For the initial unstrained condition (not shown in Fig. 14) the strain distribution is represented by a Dirac delta function. A broadening of strain distribution is observed in both RVEs with increasing strain. Broadening is more pronounced in $RVE_{CARB.}$ at all strain levels, indicating a more heterogeneous strain, by development of regions with high strain levels and others in which strain development is hindered compared with fully ferritic microstructure. It is not possible to establish a direct correspondence between experimental and simulated results, considering that the former only accounts for plastic deformation leading to GNDs (but

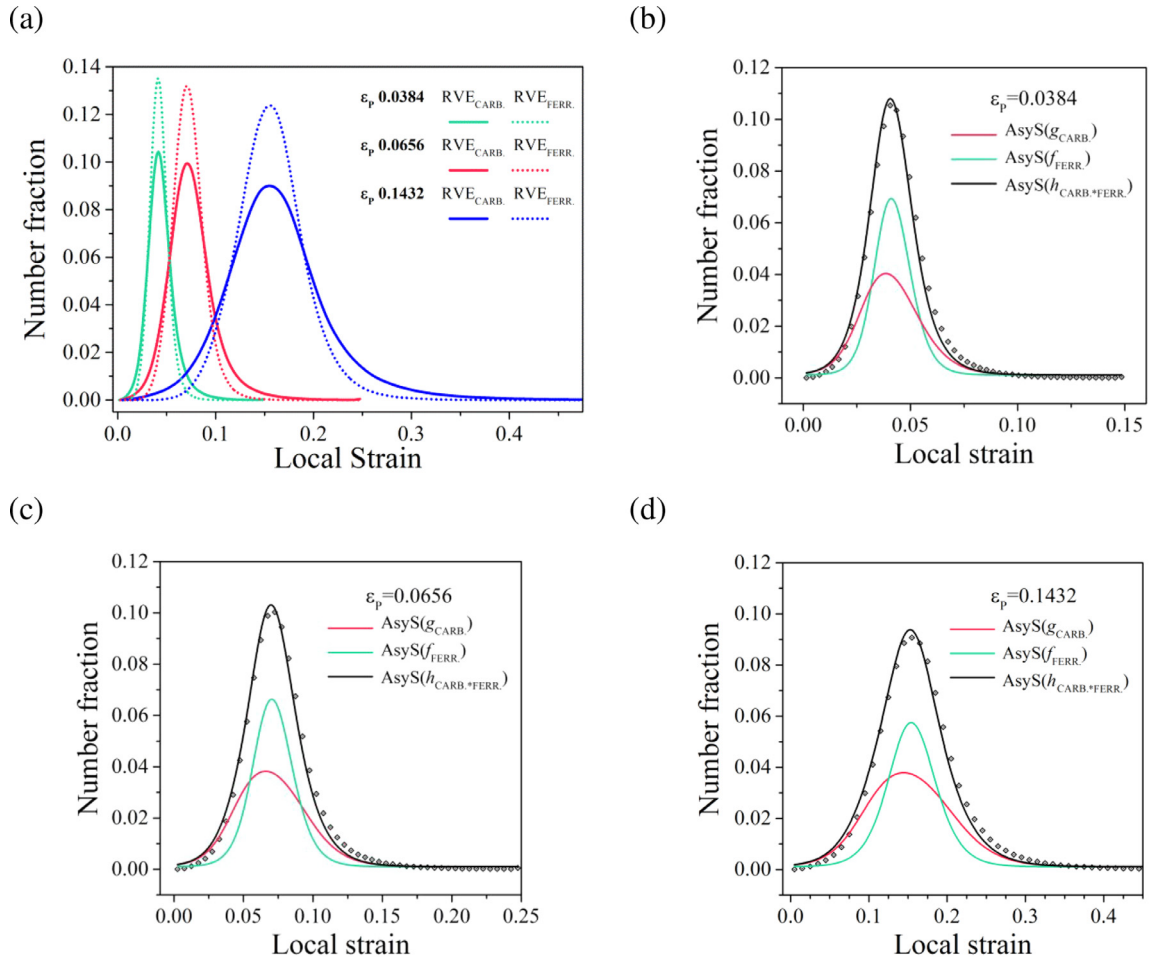

Fig. 14. (a) Histograms of the local strain distribution obtained from $RVE_{CARB.}$ and $RVE_{FERR.}$ at differen levels of plastic deformation. The number fraction corresponds to 50 bins. For shake of a better comparison, a continuous representation by connected lines is shown. (b)–(d) show the fitting results to asymmetric double sigmoidal funtion, AsyS, described in Eq. (12), of diferent contributions to local strain $g_{CARB.}$ and $f_{FERR.}$. They also shows the cumulative of both fitting curves, $h_{CARB.*FERR.}$. Diamonds represent the bins of histogram distribution of local strain in $RVE_{CARB.}$.

not due to the motion and generation of SSDs), and the latter includes in the statistics the deformation at every point in the RVE regardless the operating mechanism. Nevertheless, it can be concluded that the simulations are consistent with the experimental measurements.

The ferrite strain distribution function resulting from deformation of $RVE_{CARB.}$, h., can be decomposed in two parts: (1) f, which accounts for texture and strain incompatibilities between ferrite grains affecting the deformation of ferrite, i.e. the strain distribution function resulting from $RVE_{FERR.}$ and (2) g, which considers the effects of carbides, including the influence of carbides on the ferrite-ferrite grain interactions. The following procedure was followed in order to obtain g.. First, since $h = f * g$, where $*$ stands for convolution, g was obtained from h of $RVE_{CARB.}$ by deconvolution of f. The shapes of f and g can be considered representative of each individual effect to the global strain heterogeneities captured by the shape of h. However, the summation of the f and g areas does not correspond to the area of h. In order to circumvent this issue, f and g were fit to an asymmetric double sigmoidal function that was found to best fit both curves, defined as

$$y = \Lambda\left[\left(1+e^{-\left(x-x_c+\frac{w_1}{2}\right)/w_2}\right)^{-1}\left(1-\left(1+e^{-\left(x-x_c+\frac{w_1}{2}\right)/w_3}\right)^{-1}\right)\right] \quad (13)$$

where Λ represents the amplitude of the curve, x_c the strain at curve maximum and w_1, w_2, w_3 are parameters controlling the shape of the curve. h was then fit considering that this curve is the convolution of two asymmetric sigmoidal functions having respectively the x_c, w_1, w_2, w_3 values obtained from previous fitting to f and g. The A parameters of both curves were estimated to make the cumulative curve fit best to h. The Levenberg–Marquardt algorithm based on the χ-square minimisation method was used in the NLfit tool in OriginPro9 ® software. The resulting fitting of the different curves at different strain rates is shown in Fig. 14b, 14c and 14d. and their integrated area and full width half maximum (FWHM) in Fig. 15. The FWHM of all curves increases with increasing strain, but significantly stronger for the curve accounting for the sole contribution of carbides. This indicates a main contribution of carbides in the development of heterogeneous strains in the ferrite phase. The contribution of carbides alone to global strain is similar to that of the other effects in view of the similar integrated areas of their corresponding curves.

Fig. 16 shows equivalent Von Mises strain maps of the same section of $RVE^*_{CARB.}$ and $RVE^*_{FERR.}$ at different strain levels. A direct comparison between experimental KAM and IQ maps and the simulated strain map should be done with care. For example, translating KAM maps into strain maps will require to choose a starting point and integrate over the total domain to generate a strain map. However, KAM and IQ maps give a reasonable indication of regions where heterogeneous strain strongly develops. Upon these consid-

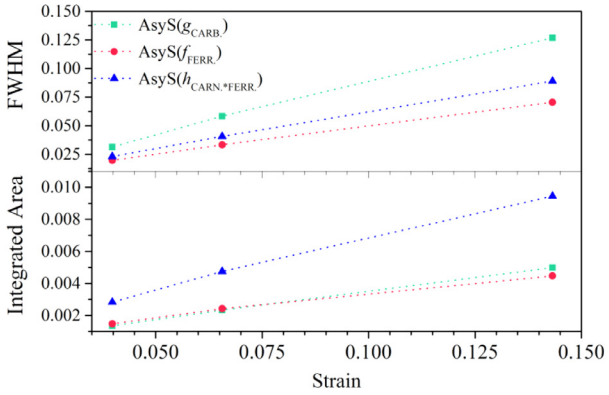

Fig. 15. Full width half maximum (FWHM) and integrated area of $g_{CARB.}$, $f_{FERR.}$ and $h_{CARB.*FERR.}$ variation with macroscopic strain.

erations, experimental observations are to some extent reproduced in RVE*$_{CARB.}$. Carbides barely deform compared to ferrite and concentrate high strain levels in their surroundings. High strain also develops at ferrite boundaries and triple junctions compared to grain interior. The effect of carbides is clearly evidenced when comparing RVE*$_{CARB.}$ to RVE*$_{FERR.}$. Strain develops more heterogeneously in RVE*$_{CARB.}$, with regions exhibiting higher strains than their RVE*$_{FERR.}$ counterparts, but also regions that deform less. This fact was already predicted upon analysing the strain distribution curves in Fig. 14a. Features resembling slip bands are recognizable from 0.0384 plastic strain in RVE*$_{CARB.}$ and a cell structure formed by band intersections develops with increasing strain in a similar fashion as experimentally observed. It should be remarked, though, that cell structure in experimental specimens can also be a consequence of small precipitates, which are absent in the microstructure of the RVEs. Strain gradients are less pronounced in RVE*$_{FERR.}$ and features resembling deformation bands are not clearly formed, although high strain values concentrate at ferrite boundaries and triple junctions. Equivalent regions in RVE*$_{CARB.}$ develop higher strain levels regardless the presence or absence of carbides, which indicates that carbides not only influence local strain directly by elastic incompatibilities with the ferritic matrix, but also the spatial interactions between ferrite grains.

5. Discussion

5.1. Assessment of micromechanical model

The conclusions extracted from a comparative analysis of modelled deformed microstructures are subjected to the intrinsic limitations of the representative volumes and the constitutive equations adopted. First remarkable issue is that the linear elastic part in the simulated curves in Fig. 13 exhibits an abnormally high Young's modulus of 275 GPa compared to the general accepted Young's modulus of steel. The direction dependence of the Young's modulus of cubic crystal system can be expressed as

$$A_{hkl} = \frac{h^2k^2 + l^2k^2 + h^2l^2}{\left(h^2 + k^2 + l^2\right)^2} \tag{14}$$

$$1/E_{hkl} = S_{11} - 2\left[S_{11} - S_{12} - \frac{1}{2}S_{44}\right]A_{hkl} \tag{15}$$

where A_{hkl} is the elastic anisotropy factor, E_{hkl} is the elastic modulus of the crystallographic plane <*hkl*> and S_{ij} are the elastic compliances. The equation relating the elastic compliances with the elastic stiffness matrix components can be found in, e.g., Knowles et al. [51]. A high population of grains oriented with <111> normal to the load direction in the RVE, with E_{111} = 306 GPa, explains the high Young's modulus obtained in the simulated tensile curves. Fig. 5 shows that as the number of ferrite grains decreases in RVE*$_{CARB.}$, the grain orientation along the {111} becomes more dominant, an unintended result of the algorithm used to assign texture to grains based on ODF. In the case of RVE$_{CARB.}$, the number of ferrite grains might be not enough to capture less intense texture components, and texture along {111} manifests more intense than that of the real material. This fact reveals the importance of the selection of an adequate number of grains with a representative texture, which was confronted in this study with limitations in computational power. Simulations with RVEs with a high number of carbides and grain boundaries are recommended for future studies. Nevertheless, simulations with a random texture RVE leads

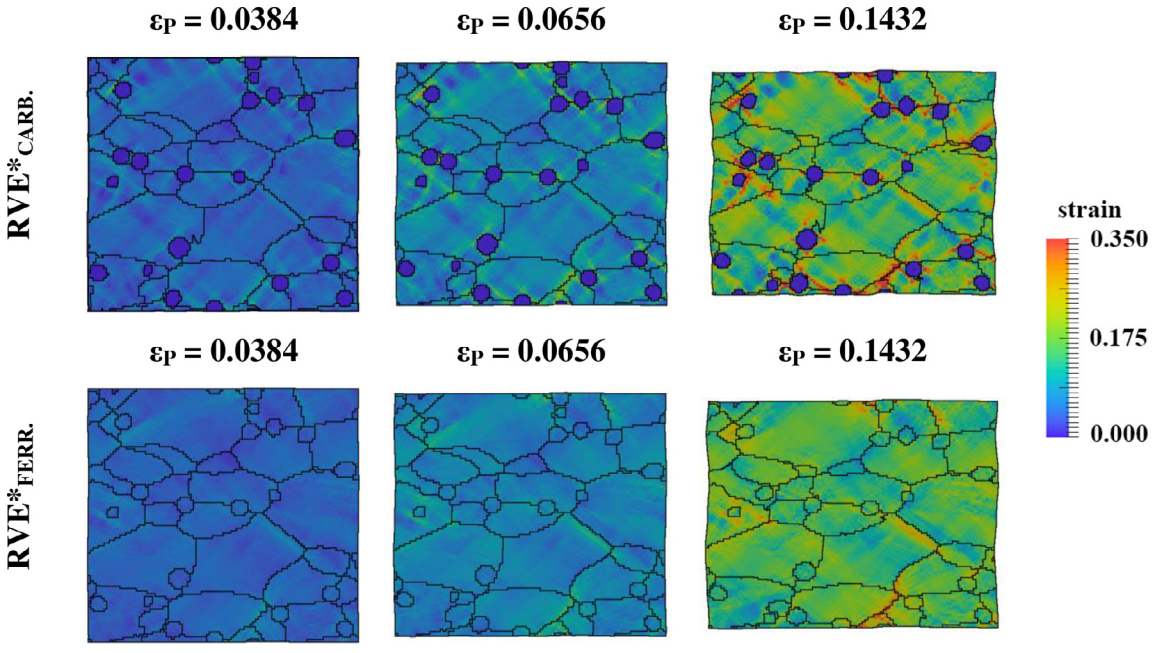

Fig. 16. Ditribution of equivalent Von Mises plastic strain at different macroscopic strain for RVE*$_{CARB.}$ and RVE*$_{FERR.}$

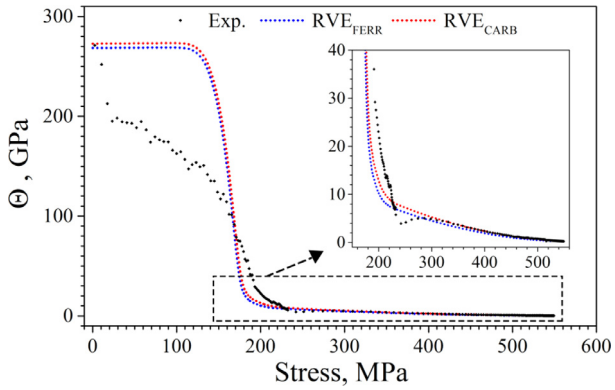

Fig. 17. Instantaneos work hardening rate, Θ, vs. stress curves obtained from experimental (Exp.) and modelled ($RVE_{CARB.}$ and $RVE_{FERR.}$) tensile tests.

to $E = 216$ MPa, which is still higher than that for the alloy, but credits the choice of C_{ij}.

Another issue arises during the transition from elastic to plastic deformation. The instantaneous work hardening, $\Theta = d\sigma/d\varepsilon$, is plotted as a function of stress in Fig. 17 for a better assessment of elastic to plastic transition according to Arechabaleta et al. [52]. In the experimental plot, an abrupt monotonic decrease of Θ below the material yield stress indicates an anelastic regime, consequence of dislocation bow-out by Orowan mechanism, but with limited dislocation glide. This trend is more progressive in AISI 420 steel than in pure iron and low alloy ferritic steel [52], which points to an effect of the carbides or the reduced ferrite grain size. Initial instantaneous modulus of around 275 GPa is attributed to inaccuracies in the strain measurement at low deformation. This value rapidly evolves to a more reasonable value of 200 GPa. Above 220 MPa stress, a change in trend is observed and Θ slightly increases to subsequently smoothly decrease to $\Theta = 0$ GPa when maximum uniform elongation is achieved. Cheng et al. [53] observed this behaviour for overaged aluminium alloys as the precipitates reached an average size at which dislocations cannot longer shear it, which it is assumed the case for large $M_{23}C_6$ carbides in AISI 420.

The modelled curves do not accurately capture the real material hardening behaviour until approximately 275 MPa, well into the plastic regime. Fig. 17 shows a hardening rate in the simulation that significantly deviates from the experimental result in the strain region below 2%. In the simulation, the initial state does not include any internal stress. However, as shown in the KAM map of Fig. 10, the initial state, without applied load, does include lattice distortion around the boundaries, which can be attributed to a misfit strain due to thermal stress during cooling in the process. The initial residual stress may assist in a plasticity initiation by dislocation nucleation/multiplication as indicated by Shimokawa et al. [54]. This can be a reason for the lower flow stress leading to the lower hardening rate as shown in Figs. 13 and 17. Since the simulation is operated in displacement-controlled mode, a given strain is compensated by plastic and elastic strains. If the microstructure does not allow the development of plastic strain, the strain is accommodated elastically, leading to a higher applied stress by Hooke's law. In the model, the early hardening behaviour is addressed by the h_0 parameter or initial hardening, which is considered constant along the individual grains. In future work, it would be interesting to incorporate a third phase with different h_0 in the RVE along the grain boundaries to consider the effect of initial strain at these locations.

However, they do recreate an abrupt decrease in Θ after a prolonged plateau maintaining the initial instantaneous modulus. This decrease cannot be attributed to a reversible anelastic behaviour, since this is not included in the modelling, but to a progressive activation of glide in differently oriented grains. Following a generalization of Schmid's law, any slip system will be active if and only if the corresponding shear stress and stress rate on that system reach critical values [55,56]. The question that arises is which stress value should be considered for the initiation of yielding. If the point in which first slip systems start to glide is selected, there are no significant differences between $RVE_{CARB.}$ and $RVE_{FERR.}$. This would indicate a negligible influence of the carbide phase at low strains, which contribution to the deformation of the artificial microstructures is only expected to be a local increase in strain due to elastic incompatibilities. However, differences in the stress values increase as the strain increases for the artificial microstructures, reaching a maximum of 18.6 MPa near maximum uniform elongation. This makes σ_y, defined as the 0.2%-offset yield stress, slightly higher in $RVE_{CARB.}$ (208 MPa) compared to $RVE_{FERR.}$ (203 MPa). However, it cannot be explained directly by classical strengthening mechanisms in the synthetic microstructures.

Phenomenological constitutive formulation suffers from the drawback that the material state is only described in terms of the critical resolved shear stress, τ_C^η, and not in terms of lattice defects population. The presence, motions, and interactions of dislocations are not explicitly identified by the model. Any specific physical contribution to hardening of GNDs is disregarded by the local crystal plasticity model. Nevertheless, if a carful interpretation is made, useful information can be extracted from the application of this model. Based on the hardening law adopted in this work, Acharya and Bassani [57] formulated that $h_{\beta\eta}$ depends both on the slips and their gradients via the incompatible lattice deformations, i.e., Nye's GND density evolution with strain, $\dot{\alpha}_{ij}$:

$$\dot{\alpha}_{ij} = e_{ijkl} \sum_{\beta=1}^{N} \dot{\gamma}^{\eta} \boldsymbol{m}_{\beta} \otimes \boldsymbol{n}_{\beta} \tag{16}$$

where e_{ijkl} denotes the alternating vector. It should be stressed here that Eq. (16) only provides a relation of the strain gradients arising by the local plasticity theory with GNDs. Under multi-slip deformation of ferrite in this study, a distinction should be made for short- and long-range character of the interaction between a mobile dislocation and the GND content. Short-range interactions may be fully accounted for in the hardening rate matrix, $h_{\beta\eta}$. The contribution to stress of long-range interactions due to the presence of GNDs can be considered to arise solely from the presence of an incompatibility. Incompatibility will develop in ferrite-ferrite and ferrite-$M_{23}C_6$ boundaries as a direct consequence of the individual orientations of grains, combined with the anisotropy of the elastic stiffness tensor. Under these assumptions, and considering that the ferrite parameters are the same, the differences observed between $RVE_{CARB.}$ and $RVE_{FERR.}$ would be due to the contribution of $M_{23}C_6$ carbides to hardening due to both long-range and short-range interactions.

The results should be also interpreted considering the limitations in the model when tackling spatial grain interactions, which affect the manner in which grains deform and rotate influencing the development of texture. An advantage of crystal plasticity finite element predictions is that they can reproduce experimental findings well. However, they are restrained to the use of a proper RVE and constitutive model as inputs. For the validation of the simulation, textures of experimental and artificial microstructures for the unstrained and 0.14 plastic strain conditions are illustrated by $\varphi_2 = 45°$ sections of the orientation distribution function (ODF) in Fig. 18 and Fig. 19, respectively. Unstrained AISI 420 steel (Fig. 18a) exhibits a typical texture of rolled and annealed iron bcc, with most intense components located approximately at {111}<112> and {554}<225> [58–60]. These orientations of the recrystallized grains are preferred for nucleation and

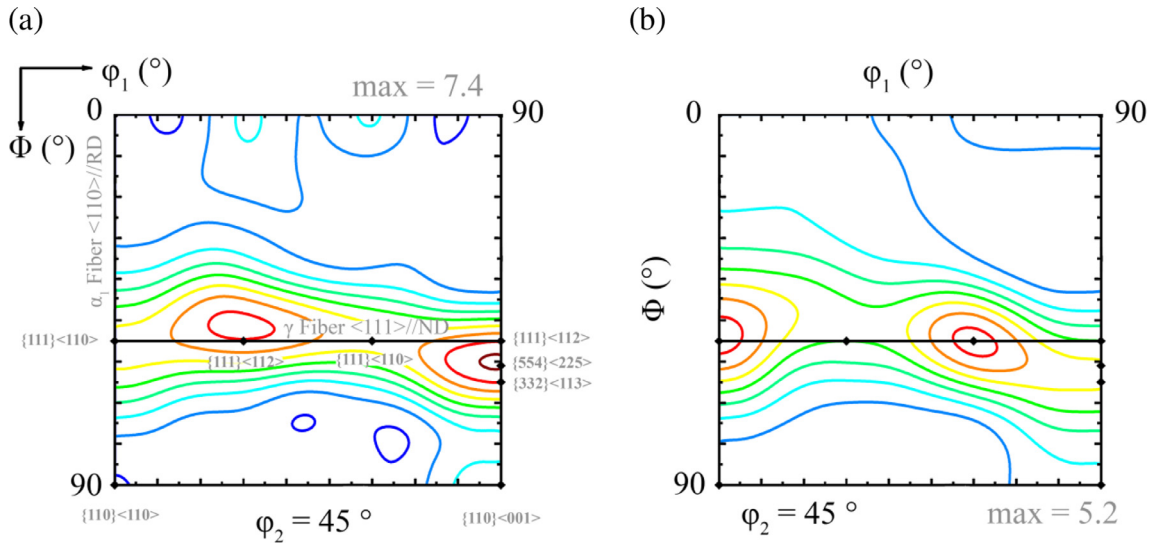

Fig. 18. $\varphi_2 = 45°$ sections ODF of AISI 420 obtained from EBSD data and TSL OIM® Analyses 6.0 software, (a) $\varepsilon_P = 0$, (b) $\varepsilon_P = 0.139$.

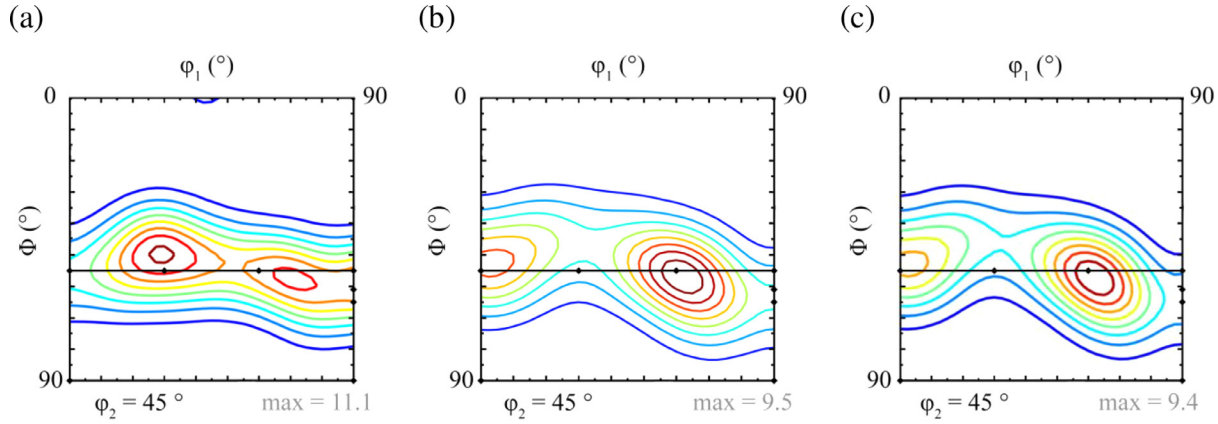

Fig. 19. $\varphi_2 = 45°$ sections ODF of obtained after DAMASK simulation and MTEX Toolbox, (a) $\varepsilon_P = 0$ ($RVE_{CARB.}$, $RVE_{FERR.}$), (b) $\varepsilon_P = 0.143$, $RVE_{CARB.}$, (c) $\varepsilon_P = 0.143$, $RVE_{FERR.}$

growth from deformed grains with orientation {112}<110> and {111}<110>. Further uniaxial deformation rotates {111}<112> and {554}<225> components preferentially to {111}<110>, but maximum intensity decreases compared to the unstrained state. Artificial microstructure texture (equal for $RVE_{CARB.}$ and $RVE_{FERR.}$), illustrated in Fig. 19a, reproduces AISI 420 steel texture reasonably well, but exhibits a more intense texture at {111}<112>. The {554}<225> component is less intense and texture is more pronounced towards {111}<110>. The deformed $RVE_{CARB.}$ and $RVE_{FERR.}$ (Fig. 19b and 9C, respectively) exhibit very similar texture, which indicates a minor effect of the relatively small fraction of $M_{23}C_6$ carbides. Textures evolve similarly to that of experimental specimen at 0.14 plastic strain, in which intensity decreases compared to the unstrained condition. Assuming the abovementioned limitations, and in view of good agreement between experimental and predicted curves and textures at high plastic strains, it can be stated that observations made in $RVE_{CARB.}$ and $RVE_{FERR.}$ would be reasonably well reproduced in equivalent real microstructures.

5.2. Effect of carbides on plastic flow

The work hardening of AISI 420 annealed microstructure, magnitude 330 MPa, is higher than that for other annealed ferritic low carbon and stainless steels, which are in the range between 100 MPa to 200 MPa [61]. This fact is explained by high density of large $M_{23}C_6$ and small MX precipitates. The effect of small ferrite grains is also significant, following from simulations with modelled full ferritic microstructure resulting in only less than 20 MPa of work hardening difference with respect to modelled microstructure containing large $M_{23}C_6$ carbides. However, the calibration of parameters for ferrite also accounted for the effect of small MX precipitates, which were not included in the simulated microstructures. Therefore, the effect of small ferrite grain size should be corroborated in other carbide free ferritic microstructures.

Large $M_{23}C_6$ carbides would also result in high initial hardening rates, which are typically observed for metal alloys with a low volume fraction of non-shearable precipitates [53]. This has been attributed to two mechanisms: (1) the storage of geometrically necessary dislocations, (2) the storage of elastic energy of the second phase. The calibrated h_0 hardening parameter is higher compared to other ferritic steels [7,37,38]. High h_0 is typical for martensitic steels with high dislocation density and small grain size [7,62]. A low initial dislocation density is assumed in annealed AISI 420 steel. Hence, high h_0 might be related to presence of carbide precipitates in present study. Further analysis was made recalibrating the ferrite properties to describe the behaviour of real material containing carbides, using this time $RVE_{FERR.}$. The only remarkable difference in the recalibrated hardening model parameters for ferrite was obtained for h_0 with a value of 2660 MPa. This variation of 130 MPa in the hardening parameter is interpreted as an excess of initial hardening, e.g. due to a higher initial density of slips sys-

tems (dislocations), required in the system to compensate for the contribution of $M_{23}C_6$ carbides to hardening. This contribution to ferrite hardening can be assumed to be short- and long-range interactions due to the excess of GNDs introduced by the carbides in $RVE_{CARB.}$.

Differences in the instantaneous hardening of $RVE_{CARB.}$ and $RVE_{FERR.}$ are evident in the stress range between 190 MPa to 400 MPa (see Fig. 17), or equivalent, up to approximately 0.05 strain. At higher plastic strains the hardening behaviour of both RVEs is equivalent. This suggests that the main contribution of large $M_{23}C_6$ carbides to hardening occurs at low plastic strain. Fleck et al. [2] argued that the dominant source of hardening at levels of plastic strain below a few percent is by the generation of long-range back stresses generated by a gradient of the strain $\boldsymbol{\alpha}$. At higher levels of plastic strain, the long-range back stresses will be relaxed by cross slip and the principal source of hardening becomes isotropic hardening associated with short-range dislocation interaction. In the hardening model, $h_{\beta\eta}$ and τ_C^{η} interdependently evolve with macroscopic plastic strain according to Eqs. (5)–(7) which complicates discerning the character of carbides interaction. However, the saturation stress is the same in $RVE_{CARB.}$ and RVE_{FERR} since this represents the physical limit to the density of dislocations that might be stored in the ferrite crystal. Therefore, the difference of 20 MPa in the ultimate tensile strength between $RVE_{CARB.}$ and RVE_{FERR} arises only due to differences in hardening below a strain of 0.05. Considering that h_0 for ferrite is the same in both RVEs, it can be deducted that observed differences in hardening arise solely from strain incompatibilities. The local crystal plasticity model does not consider extra hardening due to a long-range interaction mechanism, however it can be assumed to be based on existing theory that long-range interactions will dominate at low strains and will be more pronounced due to the strain incompatibilities introduced by carbides compared to ferrite grain boundaries. The 0.05 strain coincides with the observation of shear bands in deformed the AISI 420 microstructure as shown in Fig. 10. Wang et al. [63] demonstrated by 3D dislocation dynamics that the underlying mechanism for slip band formation is through cross-slip. Hence, the observation of shear bands can be connected to a shift in the governing hardening mechanism. The development of cross-slip might be evidenced in RVE_{CARB} by the formation of bands with high local strain (Fig. 16), which would be in agreement to observation of shear bands in the real microstructure. Byrne et al. [64], observed that single crystals containing non-shearable precipitates of the Al-Cu system immediately began deformation by polyslip rather and single slip. This can be extrapolated from RVE_{CARB} results in which the activation of multiple slip systems is demonstrated by the formation of intersecting deformation bands in ferrite grains. This contrasts with deformed RVE_{FERR} grains, in which activation of single slip seems to be predominant and ferrite grains deformed more homogeneously.

KAM continuously increases with macroscopic strain following a linear trend (see Fig. 8b), consistent with the Ashby model [42] and the observations reported by other researchers in ferritic steels [44,45]. A competition between dislocation accumulation and dynamic recovery at high plastic strains would explain the high initial instantaneous work hardening despite the rate of increase of GND density with strain remaining constant. Results with modelled microstructures in Fig. 15, show a broadening of the strain distribution also following a linear trend with a main contribution of carbides to the development of strain heterogeneities. It is also observed that carbides enhance the contribution of ferrite grain boundaries to the increase of local strain. The statistical analysis of evolution of local strain in deformed AISI 420 microstructure evidences a positive effect of carbides and grain boundaries in KAM (Fig. 11), in particular at low macroscopic plastic strain, which can be related to development of GNDs. At high plastic strain, average KAM at different parcels becomes more similar regardless the density of carbides or grain boundaries. This is explained by the formation and spread of cell structures that initiate at carbides and grain boundaries, which is consistent by a shift to predominant contribution to hardening of short range dislocation interactions. This fact does not contradict the overall more heterogeneous KAM as observed in Fig. 9a. Despite the average values KAM tending to equalise, the interquartile range widens with strain for all populations of carbides and ferrite grains as plastic strain increases.

The present study demonstrates by modelled microstructures the key role of large $M_{23}C_6$ in the formation of cell structures in ferrite grains. Cell structure would develop by occurrence of polyslip excluding the formation of easy-glide regions in a similar manner as in Ref. [64]. These cell boundaries would be formed by accumulation of dislocation tangles with similar Burgers vector [8], which evolve in low-angle subgrain boundaries, e.g. during annealing treatments or creep [13]. This study also suggests an influence of carbide position in the development of heterogeneous strains in the microstructure. Generation of artificial microstructures with controlled distribution of carbides and carbide/ferrite grain size ratio will be a powerful tool in future studies of AISI 420 steels and other materials with large precipitates.

6. Conclusions

The influence of large $M_{23}C_6$ carbides on the heterogeneous strain development in annealed 420 stainless steel was studied combining experimental results and crystal-plasticity based simulations on an artificial recreation of the microstructure. Simulations of two different 3D representative volume elements (RVE), one mimicking real ferrite-carbides microstructure and another consisting only of ferrite phase, were compared to experimental results and the following main conclusions are extracted:

(1) Modelled tensile curves, obtained after the calibration of constitutive model parameters, accurately reproduce experimental curves, although they show limitations on accurately capturing the real hardening behaviour at strains below 0.02, likely due to residual stresses observed in the material are not considered in the RVEs. The evolution of texture and local stain was also well predicted in deformed RVEs, which emphasises the importance of having a good RVE representation and confirms the role of different mechanisms of strain development in presence or absence of large $M_{23}C_6$ carbides.
(2) Results suggest that carbides provide a more effective hardening at low plastic strain as they introduce stronger strain heterogeneities compared to a purely ferritic microstructure, likely by a predominant long-range interaction mechanism. At strains around 0.05, cross-slip is evidenced in real and artificial microstructures containing carbides indicating a change in the hardening mechanism dominated by short range dislocation interactions. The hardening behaviour of ferritic and carbides-containing microstructures become similar at high plastic strain.
(3) Strain developed more heterogeneously in RVE containing carbides compared to ferritic RVE. Unlike ferritic RVE, a cell structure delimited by high local strains is formed in the RVE with carbides similar to experimental observations. Carbides not only influence local strain directly by elastic incompatibilities with the ferritic matrix, but also the spatial interactions between ferrite grains.
(4) Carbides placed at grain boundaries enhance the development of strain near ferrite grain boundaries. A statistical linear regression model shows the positive effect of ferrite grain boundaries and carbides in the development of high local strains. However, the model also reflects that development of local

strain will be mitigated in regions with high density of grain boundaries and carbides.

Declaration of Competing Interest

The authors declare that they have no known competing financial interests or personal relationships that could have appeared to influence the work reported in this paper.

Acknowledgments

The authors acknowledge Aritra Chakraborty and Philip Eisenlohr from Michigan State University for generously sharing their NM optimization code. The research leading to these results has received funding from of VMAP – ITEA 16010 project via the ITEA 3 cluster of the European research initiative EUREKA.

References

[1] A. Ma, A. Hartmaier, On the influence of isotropic and kinematic hardening caused by strain gradients on the deformation behaviour of polycrystals, Philos. Mag. 94 (2014) 125–140.
[2] N.A. Fleck, M.F. Ashby, J.W. Hutchinson, The role of geometrically necessary dislocations in giving material strengthening, Scr. Mater. 48 (2003) 179–183.
[3] C.J. Bayley, W.A.M. Brekelmans, M.G.D. Geers, A comparison of dislocation induced back stress formulations in strain gradient crystal plasticity, Int. J. Solids Struct. 43 (2006) 7268–7286.
[4] P.D. Littlewood, T.B. Britton, A.J. Wilkinson, Geometrically necessary dislocation density distributions in Ti–6Al–4V deformed in tension, Acta Mater. 59 (2011) 6489–6500.
[5] P.S. Karamched, A.J. Wilkinson, High resolution electron back-scatter diffraction analysis of thermally and mechanically induced strains near carbide inclusions in a superalloy, Acta Mater. 59 (2011) 263–272.
[6] J. Kadkhodapour, S. Schmauder, D. Raabe, S. Ziaei-Rad, U. Weber, M. Calcagnotto, Experimental and numerical study on geometrically necessary dislocations and non-homogeneous mechanical properties of the ferrite phase in dual phase steels, Acta Mater. 59 (2011) 4387–4394.
[7] C.C. Tasan, J.P.M. Hoefnagels, M. Diehl, D. Yan, F. Roters, D. Raabe, Strain localization and damage in dual phase steels investigated by coupled in-situ deformation experiments and crystal plasticity simulations, Int. J. Plast. 63 (2014) 198–210.
[8] N.A. Koneva, L.I. Trishkina, T.V. Cherkasova, E.V. Kozlov, Effect of the grain size on accumulation of scalar density of dislocations and its components in low-alloy Cu–Al, Inorg. Mater. Appl. Res. 8 (2017) 566–572.
[9] J. Jiang, T.B. Britton, A.J. Wilkinson, Evolution of dislocation density distributions in copper during tensile deformation, Acta Mater. 61 (2013) 7227–7239.
[10] E.O. Hall, The deformation and ageing of mild steel: III discussion of results, Proc. Phys. Soc. Lond. Sect. B 64 (1951) 747–753.
[11] J. Li, C. Zhang, B. Jiang, L. Zhou, Y. Liu, Effect of large-size M23C6-type carbides on the low-temperature toughness of martensitic heat-resistant steels, J. Alloys Compd. 685 (2016) 248–257.
[12] C. Revilla, B. López, J.M. Rodriguez-Ibabe, Carbide size refinement by controlling the heating rate during induction tempering in a low alloy steel, Mater. Des. (1980–2015) 62 (2014) 296–304.
[13] T. De Cock, C. Capdevila, F.G. Caballero, C. García de Andrés, Global recrystallisation model of low carbon sheet steels with different cementite contents, Mater. Sci. Eng.: A 519 (2009) 9–18.
[14] J. Vivas, C. Capdevila, E. Altstadt, M. Houska, I. Sabirov, D. San-Martín, Microstructural degradation and creep fracture behavior of conventionally and thermomechanically treated 9% chromium heat resistant steel, Metals Mater. Int. 25 (2019) 343–352.
[15] F. Roters, M. Diehl, P. Shanthraj, P. Eisenlohr, C. Reuber, S.L. Wong, T. Maiti, A. Ebrahimi, T. Hochrainer, H.O. Fabritius, S. Nikolov, M. Friák, N. Fujita, N. Grilli, K.G.F. Janssens, N. Jia, P.J.J. Kok, D. Ma, F. Meier, E. Werner, M. Stricker, D. Weygand, D. Raabe, DAMASK – The Düsseldorf Advanced Material Simulation Kit for modeling multi-physics crystal plasticity, thermal, and damage phenomena from the single crystal up to the component scale, Comput. Mater. Sci. 158 (2019) 420–478.
[16] F. Roters, P. Eisenlohr, L. Hantcherli, D.D. Tjahjanto, T.R. Bieler, D. Raabe, Overview of constitutive laws, kinematics, homogenization and multiscale methods in crystal plasticity finite-element modeling: theory, experiments, applications, Acta Mater. 58 (2010) 1152–1211.
[17] D. Caillard, Kinetics of dislocations in pure Fe. Part I. In situ straining experiments at room temperature, Acta Mater. 58 (2010) 3493–3503.
[18] R. Gröger, V. Racherla, J.L. Bassani, V. Vitek, Multiscale modeling of plastic deformation of molybdenum and tungsten: II. Yield criterion for single crystals based on atomistic studies of glide of 1/2 <111) screw dislocations, Acta Mater. 56 (2008) 5412–5425.
[19] ASTM-E8-E8M-13a, in: Standard Test Methods for Tension Testing of Metallic Materials, ASTM International, PA, United States, 2013, p. 28.
[20] K.B. Small, D.A. Englehart, T.A. Christman, Guide to etching specialty alloys, Adv. Mater. Processes 166 (2008) 32–37.
[21] L.Y. Dai, G.Y. Niu, M.Z. Ma, Microstructure evolution and nanotribological properties of different heat-treated AISI 420 stainless steels after proton irradiation, Materials (2019) 12.
[22] R. Hu, G. Bai, J. Li, J. Zhang, T. Zhang, H. Fu, Precipitation behavior of grain boundary M23C6 and its effect on tensile properties of Ni–Cr–W based superalloy, Mater. Sci. Eng.: A 548 (2012) 83–88.
[23] T.-H. Lee, Y.-J. Lee, S.-H. Joo, H.H. Nersisyan, K.-T. Park, J.-H. Lee, Intergranular M23C6 carbide precipitation behavior and its effect on mechanical properties of Inconel 690 Tubes, Metallurg. Mater. Trans. A 46 (2015) 4020–4026.
[24] Y. Xu, X. Zhang, Y. Tian, C. Chen, Y. Nan, H. He, M. Wang, Study on the nucleation and growth of M23C6 carbides in a 10% Cr martensite ferritic steel after long-term aging, Mater. Charact. 111 (2016) 122–127.
[25] J. Vivas, C. Capdevila, E. Altstadt, M. Houska, D. San-Martín, Importance of austenitization temperature and ausforming on creep strength in 9Cr ferritic/martensitic steel, Scr. Mater. 153 (2018) 14–18.
[26] K. Lücke, M. Hölscher, Rolling and recrystallization textures of BCC steels, Text. Microstruct. 14 (1991) 585–596.
[27] M.A. Groeber, M.A. Jackson, DREAM.3D: a digital representation environment for the analysis of microstructure in 3D, Integr. Mater. Manuf. Innov. 3 (2014) 56–72.
[28] M. Groeber, S. Ghosh, M.D. Uchic, D.M. Dimiduk, A framework for automated analysis and simulation of 3D polycrystalline microstructures. Part 2: Synthetic structure generation, Acta Mater. 56 (2008) 1274–1287.
[29] A. Chakraborty, P. Eisenlohr, Evaluation of an inverse methodology for estimating constitutive parameters in face-centered cubic materials from single crystal indentations, Eur. J. Mech. A. Solids 66 (2017) 114–124.
[30] J.A. Nelder, R. Mead, A simplex method for function minimization, Comput. J. 7 (1965) 308–313.
[31] J. Galán-López, P. Verleysenc, Simulation of the plastic response of Ti–6Al–4V thin sheet under different loading conditions using the viscoplastic self-consistent model, Mater. Sci. Eng. A 712 (2018) 1–11.
[32] C.P. Przybyla, B.L. Adams, M.P. Miles, Methodology for determining the variance of the Taylor factor: application in Fe-3%Si, J. Eng. Mater. Technol. 129 (1) (2007) 82–93.
[33] Y. Liu, Y. Jiang, J. Xing, R. Zhou, J. Feng, Mechanical properties and electronic structures of M23C6 (M = Fe, Cr, Mn)-type multicomponent carbides, J. Alloys Compd. 648 (2015) 874–880.
[34] J. Wang, W. Guo, H. Sun, H. Li, H. Gou, J. Zhang, Plastic deformation behaviors and hardening mechanism of M7C3 carbide, Mater. Sci. Eng.: A 662 (2016) 88–94.
[35] A. Inoue, S. Arakawa, T. Masumoto, Effect of alloying elements on defect structure and hardness of M23C6 type carbides, Trans. Jpn. Inst. Metals 20 (1979) 585–592.
[36] J.R. Cahoon, W.H. Broughton, A.R. Kutzak, The determination of yield strength from hardness measurements, Metall. Trans. 2 (1971) 1979–1983.
[37] F. Maresca, V.G. Kouznetsova, M.G.D. Geers, Reduced crystal plasticity for materials with constrained slip activity, Mech. Mater. 92 (2016) 198–210.
[38] T. Yalcinkaya, W.A.M. Brekelmans, M.G.D. Geers, BCC single crystal plasticity modeling and its experimental identification, Model. Simul. Mater. Sci. Eng. 16 (2008) 085007.
[39] D.P. Field, P.B. Trivedi, S.I. Wright, M. Kumar, Analysis of local orientation gradients in deformed single crystals, Ultramicroscopy 103 (2005) 33–39.
[40] P.J. Konijnenberg, S. Zaefferer, D. Raabe, Assessment of geometrically necessary dislocation levels derived by 3D EBSD, Acta Mater. 99 (2015) 402–414.
[41] S.I. Wright, EDAX-TSL® Software vs. 8, User Manual, EDAX Inc, Draper, UT, USA, 2016 E. Inc. 2016.
[42] M.F. Ashby, The deformation of plastically non-homogeneous materials, Philos. Mag.: J. Theor. Exp. Appl. Phys. 21 (1970) 399–424.
[43] J.B. Nelson, D.P. Riley, An experimental investigation of extrapolation methods in the derivation of accurate unit-cell dimensions of crystals, Proc. Phys. Soc. 57 (1945) 160–177.
[44] D.P. Field, C.C. Merriman, N. Allain-Bonasso, F. Wagner, Quantification of dislocation structure heterogeneity in deformed polycrystals by EBSD, Model. Simul. Mater. Sci. Eng. 20 (2012) 024007.
[45] A. Kundu, D.P. Field, Geometrically necessary dislocation density evolution in interstitial free steel at small plastic strains, Metall. Mater. Trans. A 49 (2018) 3274–3282.
[46] J. Jiang, T.B. Britton, A.J. Wilkinson, Measurement of geometrically necessary dislocation density with high resolution electron backscatter diffraction: effects of detector binning and step size, Ultramicroscopy 125 (2013) 1–9.
[47] M. Kamaya, Assessment of local deformation using EBSD: quantification of accuracy of measurement and definition of local gradient, Ultramicroscopy 111 (2011) 1189–1199.
[48] H. Askari, H.M. Zbib, X. Sun, Multiscale modeling of inclusions and precipitation hardening in metal matrix composites: application to advanced high-strength steels, J. Nanomech. Micromech. 3 (2013) 24–33.
[49] V. Taupin, R. Pesci, S. Berbenni, S. Berveiller, R. Ouahab, O. Bouaziz, Lattice strain measurements using synchrotron diffraction to calibrate a micromechanical modeling in a ferrite–cementite steel, Mater. Sci. Eng.: A 561 (2013) 67–77.
[50] S. Ma, X. Zhuang, Z. Zhao, Effect of particle size and carbide band on the flow behavior of ferrite–cementite steel, Steel Res. Int. 87 (2016) 1489–1502.

[51] K.M. Knowles, P.R. Howie, The directional dependence of elastic stiffness and compliance shear coefficients and shear moduli in cubic materials, J. Elast. 120 (2015) 87–108.
[52] Z. Arechabaleta, P. van Liempt, J. Sietsma, Quantification of dislocation structures from anelastic deformation behaviour, Acta Mater. 115 (2016) 314–323.
[53] L.M. Cheng, W.J. Poole, J.D. Embury, D.J. Lloyd, The influence of precipitation on the work-hardening behavior of the aluminum alloys AA6111 and AA7030, Metall. Materials Trans. A 34 (2003) 2473–2481.
[54] T. Shimokawaa, T. Niiyamab, M. Okabec, J. Sawakoshic, Interfacial-dislocation–controlled deformation and fracture in nanolayered composites: toward higher ductility of drawn pearlite, Acta Mater. 164 (2019) 602–617.
[55] R. Hill, Generalized constitutive relations for incremental deformation of metal crystals by multislip, J. Mech. Phys. Solids 14 (1966) 95–102.
[56] J.L. Bassani, T.-Y. Wu, Latent hardening in single crystals II. Analytical characterization and predictions, Proc.: Math. Phys. Sci. 435 (1991) 21–41.
[57] A. Acharya, J.L. Bassani, A. Beaudoin, Geometrically necessary dislocations, hardening, and a simple gradient theory of crystal plasticity, Scr. Mater. 48 (2003) 167–172.
[58] H. Pan, Y. Wan, H. Wang, X. Shen, B. Fu, D.Y. Li, Y. Dai, J. Yan, An investigation of friction coefficient on microstructure and texture evolution of interstitial-free steel during warm rolling and subsequent annealing, Crystals 9 (2019) 565.
[59] J.J. Jonas, Transformation Textures Associated with Steel Processing. in Microstructure and Texture in Steels, Springer, LondonLondon, 2009.
[60] J. Fu, K. Cui, F. Li, J. Wang, Y. Wu, Texture and anisotropic mechanical properties of ferritic stainless steel stabilized with Ti and Nb, Mater. Char. 159 (2019) 110027.
[61] M. Cortie, et al., Ferritic stainless steels, in: K.H.J. Buschow, et al. (Eds.), Encyclopedia of Materials: Science and Technology, Elsevier, Oxford, 2001, pp. 3037–3039. Editors.
[62] F. Maresca, V.G. Kouznetsova, M.G.D. Geers, On the role of interlath retained austenite in the deformation of lath martensite, Model. Simul. Mater. Sci. Eng. 22 (2014) 045011.
[63] Z.Q. Wang, I.J. Beyerlein, R. LeSar, Slip band formation and mobile dislocation density generation in high rate deformation of single FCC crystals, Philos. Mag. 88 (2008) 1321–1343.
[64] J.G. Byrne, M.E. Fine, A. Kelly, Precipitate hardening in an Aluminium–Copper Alloy, Philos. Mag. 6 (1961) 1119–1145.